A coupled in-situ measurement of temperature and kinematic fields in Ti-6Al-4V serrated chip formation at micro-scale

Mahmoud Harzallah, Thomas Pottier, Rémi Gilblas, Yann Landon, Michel Mousseigne, Johanna Senatore

A coupled in-situ measurement of temperature and kinematic fields in Ti-6Al-4V serrated chip formation at micro-scale

M. Harzallah[a], T. Pottier[a*], R. Gilblas[a], Y. Landon[b], M. Mousseigne[b], J. Senatore[b]

[a] Institut Clément Ader (ICA), Université de Toulouse, CNRS, Mines Albi, UPS, INSA, ISAE-SUPAERO, Campus Jarlard, 81013 Albi CT Cedex 09, France

[b] Institut Clément Ader (ICA), Université de Toulouse, CNRS, Mines Albi, UPS, INSA, ISAE-SUPAERO, 3 rue Caroline Aigle, 31400 Toulouse, France

KEYWORDS

Primary shear zone
Digital image correlation
Infrared Thermography
micro scale
Fast imaging

ABSTRACT

The present paper describes and uses a novel bi-spectral imaging apparatus dedicated to the simultaneaous measurement of kinematic and thermal fields in orthogonal cutting experiment. Based on wavelength splitting, this device is used to image small scale phenomenon (about $500 \times 500 \mu m$ area) involved in the generation of serrated chips from Ti-6Al-4V titanium alloy. Small to moderate cutting speeds are investigated at 6000 images per second for visible spectrum and 600 images per second for infrared measuresments. It allows to obtain unblurred images. A specific attention is paid to calibration issue including optical distortion correction, thermal calibration and data mapping. A complex post-processing procedure based on DIC and direct solution of the heat diffusion equation is detailed in order to obtain strain, strain-rate, temperature and dissipation fields from raw data in a finite strains framework. Finally a discussion is addressed and closely analyzes the obtained results in order to improve the understanding of the segment generation problem from a kinemtatic standpoint but also for the first time from an energetic standpoint.

Introduction

The constant interest in understanding and mastering the machining processes has led researchers to focus more and more closely on the cutting phenomeon. In recent years, various modelling attemps has met with the need of reliable measurements to either discriminate and/or validate models [37]. The use of *post-mortem* analysis such as chip morphology and SEM analysis [57, 67, 17, 61, 60] remains the most common approach. Force components measurement in real time trough Kistler dynamometer is also very popular and has become almost dogmatic in machining research [53, 33]. Temperature measurement using thermo-couples inserted either in the part or in the tool insert has also been investegated to register macro scale heat generation [24]. The use of such global quantities (chip morphology, cutting force and tool temperature) has proven worthy but limits the understanding of local phenomena such as strain distribution and temperature generation.

To overcome this very issue, some studies have been dedicated to the assessement of *in-situ* measurement of thermomechanical quantities. The use of Quick Stop Devices has been widely developped in the machining field with some intresting results [12, 34, 30]. More recently, full-field measurement techniques have been successfully implemented for machining purpose. They offer a real-time and *in-situ* insight of the thermomechanical fields through surface measurements. Such data exhibit of course a different nature from those within the bulk of the material but remain valuable either for phenomena understanding or for model validation. Performing full-field measurements of any nature in cutting conditions exhibits two major difficulies *i)* the size of the observed area and *ii)* the rapidity with which the phenomenon occurs. These papers can be sorted in two main categories: strains measurements and infrared (IR) temperature measurements.

Though strain measurements at micro-scale are well documented in a SEM environnement [27, 21, 52], the speed requirement in cutting condition has prevented researchers to adopt this approach to obtain experimental data. Few studies have focused on such measurement, in quasi-static or dynamic conditions, through optical microscopy [29, 42]. Indeed, optical microscopy can easily be coupled with high speed imaging and thus offer a way to work around the two difficulties mentioned in the above. The use of Digital Image Correlation (DIC) has enabled the computation of strains and strain rates at microscale and low cutting speed ($V_c = 6.10^{-4} m.min^{-1}$) along continuous chips in [13] and at higher speed ($V_c = 6\ m.min^{-1}$) in serrated chips in [15, 44]. Nevertheless, this technique requires unblurred images and is thus often used at low-to-moderate cutting speed. At higher cutting speed, Particle Image Velocimetry (PIV) is often preferred eventhough it cannot be used for serrated chips [19, 23, 22]. One noticeable exception is the work of Hijazi and Madhavan [28] which have developed a complex dedicated device composed of four non-intensified digital cameras set in dual frame mode to perform a 4 unblurred images ac-

*Tel. +33 (0)5 63 49 30 48
e-mail: thomas.pottier@mines-albi.fr
www.institut-clement-ader.org

quisition at 1 MHz and thus use DIC to retreive strains. More recently, the improvement of high-speed camera spatial resolution enable Baizeau *et al.* [6] to perform DIC at higher cutting speed ($V_c = 90\ m.min^{-1}$) , this work is not directly focused on the chip formation but rather on residual stresses in the generated surface and is thus performed at a lower magnification.

Temperature measurement at tool tip within the infrared waveband have been investigated in the early 2000's by various works includig the pioneer work of [47] which uses IR pyrometry. However, thermographical studies are very seldom at high magnification. The completion of thermal measurments by corresponding kinematic measures at the same location has been adressed at micro scale by Bodelot et al. [8] with a spatial resolution of $21\mu m/pixel$ for the IR frames. The work of Arrazola *et al.* in [3, 2] also presents thermal measurement in the mid-wave IR band ($3-5\mu m$) using a home developped IR-microscope. It allowed the measurement of temperature fields with a resolution of $10\mu m/pixel$ and an exposure time of $2ms$, at a cutting speed of $400m/min$. Others authors have developed various experimental apparatus to obtain temperature fields at high cutting speeds (above $100m.min^{-1}$) for continuous chips [54, 18, 32, 59, 5]. At such cutting speed, the scale of the problem imposes to use high exposure time, therefore, the obtained images are blurred (time-convoluted) and can thus only be processed when a thermal steady state is reached. The simultaneous measurements of strains and temperatures through the same optical path have been first performed by [4, 63]. The authors use Schwarzschild reflective optics to acheive a 15X magnification and a cold mirror reflects the visible light to a visible camera and transmits infrared light to a mid-wave thermal camera. More recently Zhang *et al.* [66] have proposed a dual camera measurement of serrated chip generation using a two side configuration. This technique, well known for tensile tests proposes to capture visible images on one side of the sample and IR-fields on the other side. Authors acheive the acquisiton of thermal images at $60Hz$ with a spatial resolution of $25\mu m/pix$. Accordingly, only small cutting speed $2-4m/min$ are investigated. Finally the work of [26] presents thermal measurement at very small intergation time ($10\mu s$) and $700Hz$ in the midwave IR band, this allows to obtain unblurred and transient thermal images with a resolution of $33\mu m/pix$ and a cutting speed up to $100m.min^{-1}$.

1 Experimental Setup

1.1 Orthogonal cutting apparatus

Tests are performed in othogonal cutting configuration using a dedicated device made of a fixed tool and a linear actuator. This latter is fixed on the working plate of a conventionnal milling maching while the tool is fixed on the spindle head (see Fig.1). The feed is set to $f = 250\mu m$ using the Z-axis wheel. The chosen cutting tools are made from uncoated carbide and exhibit a rake angles of $0°$. The depth of cut is $d = 2.7mm$, the length cut is $120mm$ and the cutting speeds are ranging from $3m.min^{-1}$ to $15m.min^{-1}$. The typical geometry of the segments generated at these two cutting speeds is depicted in Fig.2d. The three components of the cutting force are recorded through a Kistler dynamometer.

1.2 Imaging apparatus

The proposed imaging device is inspired by the one presented in [4]. The key feature being a spectral separation of the incoming flux though a cold mirror that enables imaging at two different wavelengths, one dedicated to visible images (for DIC purpose) and the other to IR images (temperature measurments). The chosen configuration is slightly different in the present paper since the IR flux is here focused by reflection along the optical path. An off-axis parabolic mirror is used instead of a germanium tube lens thus preventing from chromatism throughout the IR spectrum ($0.9\mu m - 20\mu m$).

Lighting is performed from two high power LEDs ($1040lm$) one is embedded in the imaging system and provide diffuse axial illumination, the other is set outside and is focused directly on the sample thus providing a directional illumination. This latter is also added a low-pass filter to prevent stray IR illumination.

The camera on the visible optical path is a Photron Fastcam SA3 set at $6000fps$ and an exposure time of $25\mu s$. The image resolution is 512×512 pixels.

The dimensioning of the thermographic line depends on the expected thermal range. Recent works, in the field of orthogonal cutting [5, 59], with different cutting conditions (speed, angle and material), provides a glance at the expected temperature range of $T_{min} = 200°C$ to $T_{max} = 550°C$. In order to choose the most suited detector, it is classical to refer to the cross-checking of Planck's laws calculated at the two extremes temperatures of the range (Eq.1). Indeed, for a blackbody at a given temperature, 95% of the emitted flux is between $0.5\lambda_{max}$ and $5\lambda_{max}$, where λ_{max} is provided by Wien's displacement law.

$$\begin{cases} \lambda_1 = 0.5\dfrac{2898}{T_{min}} \\ \lambda_2 = 5\dfrac{2898}{T_{max}} \end{cases} \quad (1)$$

Therefore, the optimal spectral band for this temperature range is $[3.1 - 17.6]\mu m$. The commercially available detector offers wavelength range of $[3-5]\mu m$ for InSb or MCT detectors (Mid-Wave IR) or $[8-12]\mu m$ for microbolometer. In the present paper, the ability of Mid-Wave IR cameras to reach higher acquisition rates, up to 9 kHz with sub-windowing mode, have led to consider this latter type of detector.

Accordingly, the camera on the IR optical path is a FLIR SC7000 set at $600fps$ and an exposure time of $50\mu s$. The detector is sub-windowed at 1/4 in order to increase the amount of frames per second. It receives radiations through the 1mm-thick silicon beam-splitter of which the measured average transmittance is $T_\lambda \approx 0.66$ for wavelengths ranging from $3\mu m$ to $5\mu m$. The IR-image resolution is 160×128 pixels.

1.3 Material and samples

The studied material is Ti-6Al-4V titanium alloy, it presents two advantages in the scope of this study: it is industrially machined at relatively low cutting speed (typ. below $60m.min^{-1}$) and it is known to generate serrated chips even at very low cutting speed [44]. This latter feature being related to the poor thermal conductivity of titanium alloys (typ. below 10 $W.m^{-1}.K^{-1}$). The microstruture has been investigated through SEM and exhibits almost equiax grains with an average size of $19.2\mu m$. The observed surface of the sample

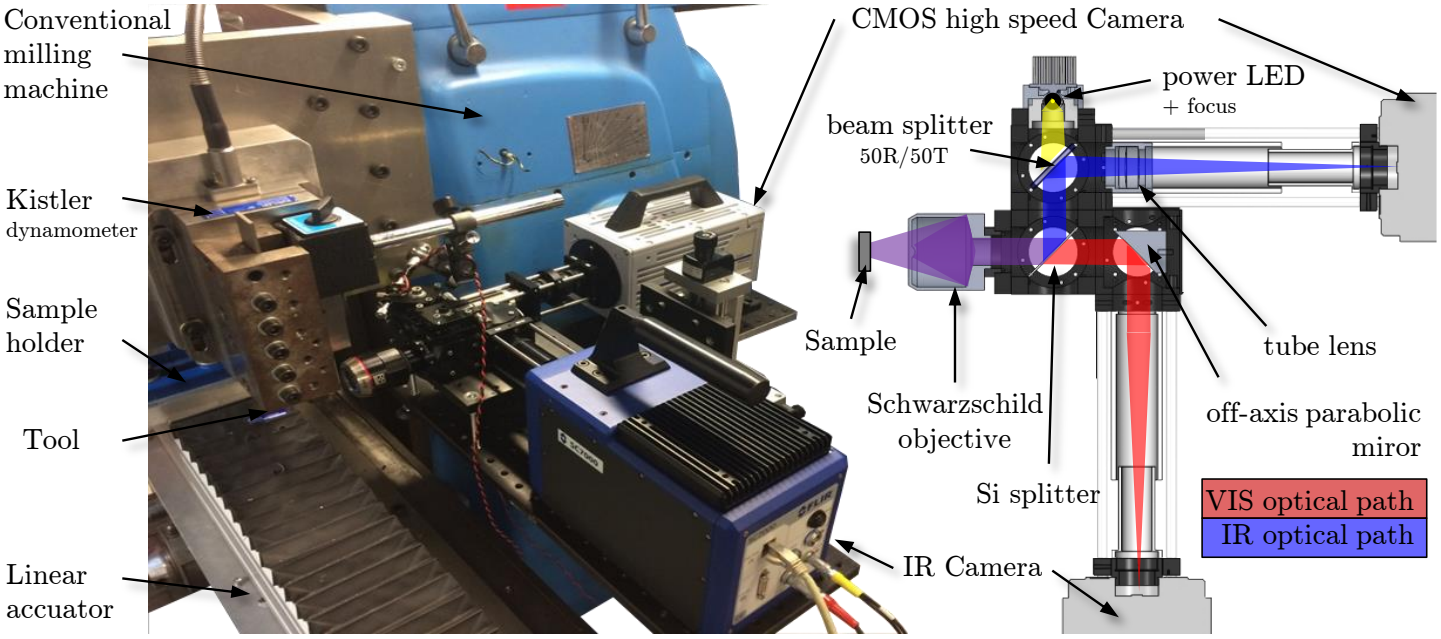

Figure 1: *a)Orthogonal cutting device and imaging apparatus. b) Schematic of the VIS-IR imaging apparatus*

is polished and etched to exhibit microstructure, this matter being used as a *natural* speckle for DIC (Fig.2a-b).

With such surface treatment, the spectral emisivity of the sample is measured from Fourier transform infrared spectroscopy. The emissivity spectrum is depicted in Fig.2c. The spectral emissivity ϵ_λ is here assumed to equal its average value over the wavelentgh range of the camera denoted ϵ. It is also assumed to remain constant within the considered temperature range [20].

The mass density ρ, the specific heat C_p and the thermal conductivity k are functions of the temperature. According to [7, 9], they are chosen to evolve linearly in-between the boundaries given in Tab.1.

2 Calibrations and optical caracterizations

2.1 Metric calibration

The size of the observed area and the amount of optical transmission from object to detectors leads to question either the exact magnification of the apparatus and the possible distortions along both visible and IR optical paths.

For magnification assessement purpose, images of calibrated lines (50 *lpm* and 31.25 *lpm*) were captured by both cameras (see Fig. 3a-d). Then a Fast Fourrier Transform of the image provide the pixel period of the pattern which lead to a metric ratio of $1.133\mu m/pixel$ for the visible camera (Photron Fastcam SA3) and knowing that the pixel pitch of this camera is $17\mu m$, the obtained magnification is $M_{vis} \approx 15.00$. The same procedure applied to the IR optical path leads to a metric ratio of $1.981\mu m/pixel$ and a magification of $M_{IR} \approx 15.14$ (detector pitch $\approx 30\mu m$).

2.2 Distortions correction

For distortion purpose, image pairs exhibiting rigid body motion along X and Y axis (the horizontal and vertical axis of the image frame respectively) are captured by both camera. The sample is being translated using a two-axis micrometric translation stages for a prescribed translation of $u_x^{pres} = 50\mu m$, then $u_y^{pres} = 50\mu m$. DIC is then performed between these images in order to assess the imposed displacement such that:

$$\begin{cases} \delta_x(\mathbf{X}) = u_x^{meas}(\mathbf{X}) - u_x^{pres} \\ \delta_y(\mathbf{X}) = u_y^{meas}(\mathbf{X}) - u_y^{pres} \end{cases} \tag{2}$$

where $\delta_x(\mathbf{X})$ and $\delta_y(\mathbf{X})$ are the components of the disortion field. Thus, assuming that optical distortions are zero at the center of the image ($\delta_x(0,0) = \delta_y(0,0) = 0$), the value of the constant u_{pres} can be assessed and the distortions estimated. Fig.3b-e reads the shape and magnitude of $\delta_x(\mathbf{X})$ and $\delta_y(\mathbf{X})$ for both visible and infrared imaging. Finally, these noised distortion fields are approximated through the model presented in [62] and used for DIC purpose in [43]. This latter proposes to approximate the distortions through the correction of radial, decentering and prismatic components as follows:

$$\begin{cases} \tilde{\delta}_x(\mathbf{X}) = x\left(r_1\rho^2 + r_2\rho^4 + r_3\rho^6\right) + 2d_1xy + d_2\left(3x^2 + y^2\right) + p_1\rho \\ \tilde{\delta}_y(\mathbf{X}) = y\left(r_1\rho^2 + r_2\rho^4 + r_3\rho^6\right) + 2d_2xy + d_1\left(x^2 + 3y^2\right) + p_2\rho \end{cases} \tag{3}$$

where $\rho = \sqrt{x^2 + y^2}$ is the distance to the optical center. A simplex optimization algorithm is used to estimate the six parameters of each model and resulting distortion fields are depicted in Fig.3c-f. It can be seen that the optical distortions exhibit similar order of magnitude for the two imaging wavelengths although the mirrors alignements issues lead to different shapes of the distortion fields. All subsequent displacement and temperature measures presented in this paper are corrected accordingly.

2.3 Image and speckle quality

No special treatment is applied on the sample surface, and the visible microstructure is used as a spekle for the DIC

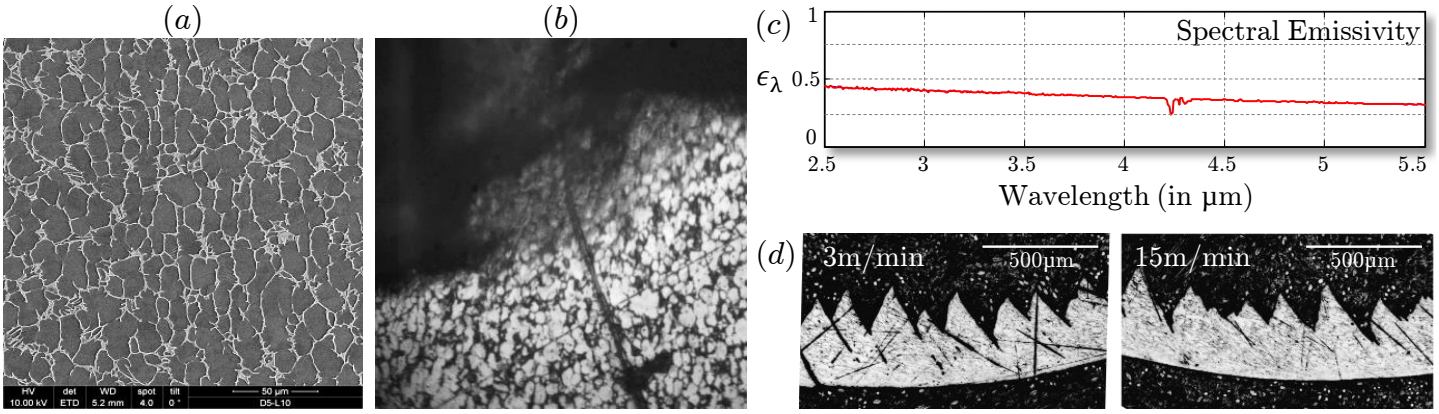

Figure 2: *(a) SEM image of a typical Ti-6Al-4V equiax microstructure. (b) Microstructure as-seen from the visible imaging line. The texture is used as a speckle for DIC. (c) Mid-wave infrared emmission spectrum of the sample surface. (d) Typical chip geometry obtained at* $3m.min^{-1}$ *and* $15m.min^{-1}$.

	ρ $kg \cdot m^{-3}$	ϵ —	C_p $J \cdot kg^{-1} \cdot K^{-1}$	k $W \cdot m^{-1} \cdot K^{-1}$
$20°C$	4450	0.37	560	6.7
$550°C$	4392	0.37	750	9.7

Table 1: Chosen material parameters for Ti-6Al-4V [7, 9, 20].

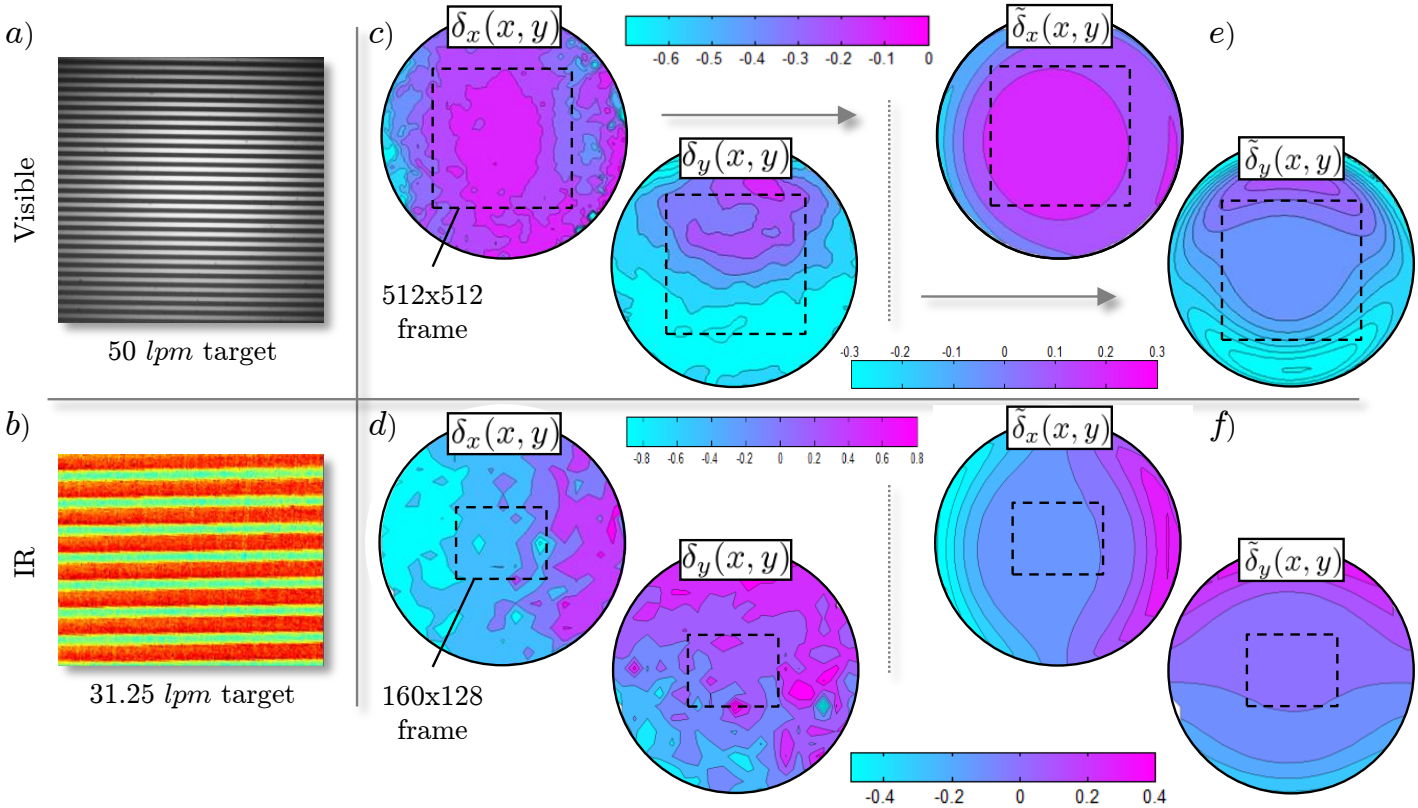

Figure 3: *a) and b) Visible and infrared images of calibrated targets of* 50 *lines per millimeter*(lpm) *and* 31.25 lpm. *c) and d) Shapes and magnitudes (in pixel) of the measured distortion fields along* x *and* y *axis for the visible and IR optical path. e) and f) Approximation of the distortion fileds from the model presented in (Eq.3). Results in pixel.*

algorithm. Estimating the measurement uncertainties of speckle related DIC techniques, is known to be a complex task [10, 40]. Lots of studies have been addressed in this field and the point of the present paper is not to discuss any further in this matter. Hence two estimation approaches are here adressed in order to assess the most suited subset size.

The first approach tested here is the so-called *Mean Intensity Gradient* [39], it provides an estimation of displacement precision (standard deviation). In the present work the image MIG is $\delta_f = 10.52$, the measurement noise is assessed from the substraction of two motionless images and its standard deviation equals $\sigma = 3.53\ pix$. Hence the standard deviation of the displacement can be approximated from:

$$std(u) \approx \frac{\sqrt{2}\sigma}{n * \delta_f} \tag{4}$$

where n is the subset size (in *pixel*). Hence, assuming a chosen subset size of $16 \times 16\ pix$, the expected standard deviation of the measured displacements is about $0.03\ pix$.

The second approach is the use of rigid body motion such as detailed in [56]. This approach is close to the one used in section 2.2. Two images exhibiting a translation motion are captured and displacement are computed and compared to the imposed one. It allows assessing both precision (random error) and accuracy (systematic errors) though this latter requires to know the accuracy of the translation stage. For this reason, only the random error is here estimated and equals $0.035\ pix$ for a subset size of $16 \times 16\ pix$. The two approaches provides approximatively the same magnitude of the dispersion. Hence, cumulating such error over 50 images lead to an maximal error or $1.5\ pix$ and therefore lead to errors on strain below 10% (if a $16 \times 16\ pix$ extensiometric basis is used).

2.4 Thermal calibration

Small scale calibration of IR cameras remains a challenging task for the thermography community. Either a specific lens is designed for microscopic observation, and calibration is then classical [49], or the camera is used without lens and the incoming radiation is focused on the detector array [31]. However, the approach presented in this latter work performs the calibration of the thermal flux ratio at two different wavelengths (bichromatic thermography), not an absolute one. In the present paper, among the two imaging paths, only one is in the infrared spectrum and thus prevents from the use of the bichromatic approach. The goal is then to perform an accurate thermal calibration (with the smallest interpolation error), at small scale. To do so, several precautions must be respected.

First of all, and as each pixel exhibits a different spectral and electronical response than its neighbours, a Non Uniformity Correction (NUC) is necessary. The method used in this paper is the Two Point Correction (TPC), which classically corrects the offsets ϕ and gains K of each pixel of coordinate $\mathbf{X}$ on the average response over every pixels. The relation between the output current of a given pixel and the read digital level is given by

$$I_d(\mathbf{X}, T) = K(\mathbf{X}) I_{current}(\mathbf{X}, T) + \phi(\mathbf{X}) \tag{5}$$

For calibration sake, two input images are required: a dark and a bright image. They are obtained by placing an integrating sphere (Optronics Laboratories OL400) in front of the camera and adjusting the lamp supplying current (see Fig.4a).

The second step of the calibration procedure is the thermal calibration. This step consists in visualizing a blackbody at different temperatures with the camera, and to choose and parametrize a model which best fits the experimental points (digital level versus temperature). The chosen model is the so-called effective extended wavelength model proposed by [51], which is recalled hereafter :

$$I_d^0(T) = K_w exp\left(-\frac{C_2}{\lambda_x T}\right) \quad \text{with} \quad \frac{1}{\lambda_x} = a_0 + \frac{a_1}{T} + \frac{a_2}{T^2} \tag{6}$$

where $I_d^0(T)$ is the averaged signal provided by the pixels viewing the blackbody at a temperature T. K_w, and the a_i are the radiometric parameters. Then the parameters identification is performed through the use of a black body set at 10 temperatures T_i ranging from $20°C$ to $550°C$ (Fig.5b):

$$log\left(I_d^0(T_i)\right) = log\left(K_w\right) - \frac{C_2 a_0}{T_i} - \frac{C_2 a_1}{T_i^2} - \frac{C_2 a_2}{T_i^3} \tag{7}$$

At small scales, an important source of error is the Size of Source Effect (SSE), which includes the illumination of the detector array by stray light and detector overwhelming [64]. It is then necessary to install a pinhole between the black body and the camera. The obtained image with a $200\mu m$ pinhole is depicted in Fig.4b, only the illuminated pixels are used for calibration. It is also verified with other pinholes ($100\mu m$ and $50\mu m$) that the incoming flux is no longer affected below $200\mu m$.

A 3^{rd} degree polynomial fit is then used to assess the radiometric parameters (error to the black body measurement are depicted in Fig.5c). The absolute error is always inferior to $7°C$, and is higher for low temperatures, where the detectivity of the pixels becomes very low (i.e. the photoresponse versus the flux of each pixels behaves non-linearly).

Once the calibration performed, in the measurement step, the emissivity must be known to infer true temperature, as defined in the following equation :

$$\epsilon(T) = \frac{I_d(T)}{I_d^0(T)} \quad \Rightarrow \quad I_d^0(T) = \frac{I_d(T)}{\epsilon(T)} \tag{8}$$

Combining Eq.(7) and Eq.(8) then gives

$$log\left(\frac{I_d(T)}{\epsilon(T)}\right) - log\left(K_w\right) + \frac{C_2 a_0}{T} + \frac{C_2 a_1}{T^2} + \frac{C_2 a_2}{T^3} = 0 \tag{9}$$

where $\epsilon(T) = \epsilon$ is assumed to be constant over the considered temperature range [20]. The computation of the true temperature T at each pixel from the measured intensity $I_d(T)$ is obtained by solving this latter equation. In practice, this is performed through the Cardano's method.

3 Measurement Post-processing

3.1 Digital Image Correlation

The DIC computations has been performed with 7D software [58]. The quality of the obtained images have led to consider the use of incremental correlation [41, 55]. This choice relies on several considerations: very significant strains, microstructure transformation, out-of-plane motion, material decohesion and changing lighting (disorientation). Therefore, the likeness of image $no.1$ and n is poor and prevent from a

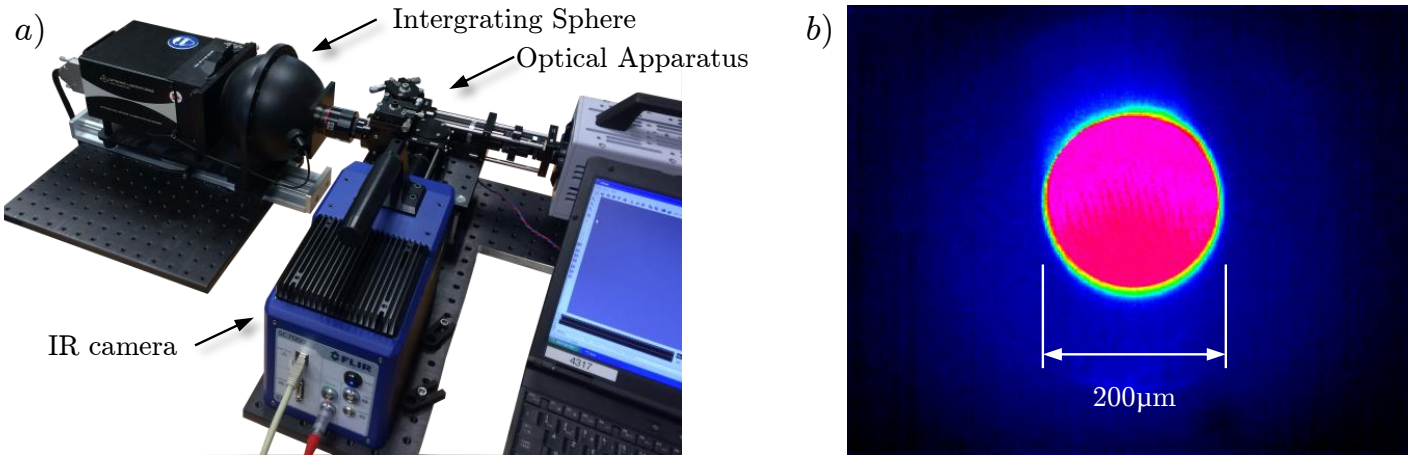

Figure 4: a) NUC correction using integrating sphere setup. b) Infrared image of the blackbody at $300°C$ through a $200\mu m$ pinhole (image at full frame 320×256 pixels).

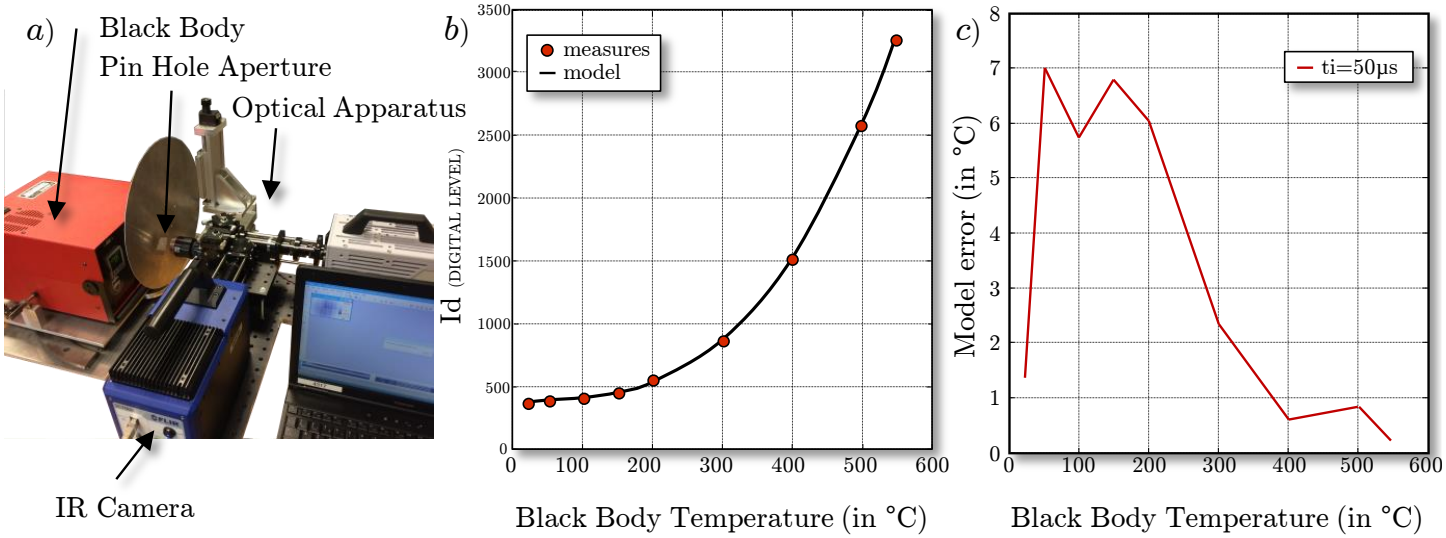

Figure 5: *a) Experimental setup for black body measurement. b) Camera signal as a function of blackbody temperature and correponding fit. c) Fit error of the black body measurements* $I_d^{measured} - I_d^{fit}$.

straight forward use of classical DIC. The matching of image $n-1$ and n is obtained with better results than images $no.1$ and n. The counterpart is that such incremental approach requires serveral numerical processings in order to compute the cumulated displacements and strains. Fig.6 depicts the resolution scheme used to retreive global displacement. Indeed, in such resolution scheme, the incremental displacements Δu_k are obtained (in pixel) at nodes of the correlation grid so that:

$$\Delta \mathbf{u}_k\left(\mathbf{X}_k\right) \tag{10}$$

where $\mathbf{X}_k = (X,Y)_k$ are the correlation grid coordinates (identical for every image in the image coordinate system but different in the local coordinate system), k being the image number. Accordingly, $\mathbf{X}_0 = \mathbf{x}_0 = (X,Y)_0$ is the intial coordinates of the tracked points. This only information does not enable the estimation of strains (whether in initial or final configuration) since material tracking can not be achieved, cumulating strain and different location is just not right. The evaluation of the deformed coordinates $\mathbf{x}_k = (x,y)_k$ at every step/images of the deformation process is performed incrementally through triangular bi-cubic interpolation.

$$\mathbf{x}_k = \mathbf{x}_{k-1} + \Delta \mathbf{u}_k\left(\mathbf{x}_{k-1}\right) \tag{11}$$

with

$$\Delta \mathbf{u}_k\left(\mathbf{x}_{k-1}\right) = \sum_{i=1}^{3} \phi_i(\mathbf{x}_{k-1}) \times \Delta \mathbf{u}_k\left(\mathbf{X}_k\right) \tag{12}$$

where the ϕ_i are classical triangular cubic shape functions. Finally the total cumulated displacement is then obtained as:

$$\mathbf{u}_k\left(\mathbf{x}_k\right) = \mathbf{x}_k - \mathbf{X}_0 \tag{13}$$

3.2 Strain Computation

The point of the present experiment is to offer a straight forward comparison of the local mechanical fields between experimental conditions and numerical simulations. For this purpose, strain fields are computed from the observed displacements. In a finite strain framework the polar decomposition of the strain gradient tensor at instant k states

$$\mathbf{F} = \mathbf{RU} = \mathbf{VR} \tag{14}$$

where $\mathbf{R}$ is the rotation matrix, and $\mathbf{U}$ and $\mathbf{V}$ are symmetric matrices describing the deformations. In most finite element softwares, explicit solvers return various measures of strains. However Eulerian strains such as the Hencky's strain $\mathbf{H}$ (a.k.a. logarithmic strain) or the so-called Swainger's strain $\mathbf{N}$ (a.k.a. nominal strains) are usually prefered in such configuration [1]. Hence, experimental strain measures are obtained from:

$$\mathbf{H} = ln\mathbf{V} \qquad \text{and} \qquad \mathbf{N} = \mathbf{V} - \mathbf{I} \tag{15}$$

where $\mathbf{I}$ stands for the identity matrix. The computation of the strain gradient tensor thus becomes the only prerequisite for strains assessement and is performed from

$$\mathbf{F}_k = \nabla_{\mathbf{X}_0}\mathbf{u}_k + \mathbf{I} \tag{16}$$

The space derivative in (Eq.16) leads to a significant issue in experimental conditions: the presence of noise on the measure of u_k. In order to address this issue, a filtering method should be applied on u_k prior to any calculation. For this purpose, a modal projection approach is chosen such as described in [45] and allows to approximate the displacement by:

$$u_k(\mathbf{X}_0) \approx \left(\sum_{p=1}^{N} \alpha_{xp} Q_p(\mathbf{X}_0) \ , \ \sum_{p=1}^{N} \alpha_{yp} Q_p(\mathbf{X}_0) \right) \tag{17}$$

where the $Q_p(\mathbf{X})$ are the N first eigen modes of a shell square plate. The α_p are the corresponding modal coordinates. The gradient then reads:

$$\nabla_{\mathbf{X}_0}\mathbf{u}(\mathbf{X}_0) \approx \begin{pmatrix} \sum_{p=1}^{N} \alpha_{xp} \frac{\partial Q_p(\mathbf{X}_0)}{\partial X} & \sum_{p=1}^{N} \alpha_{xp} \frac{\partial Q_p(\mathbf{X}_0)}{\partial Y} \\ \sum_{p=1}^{N} \alpha_{yp} \frac{\partial Q_p(\mathbf{X}_0)}{\partial X} & \sum_{p=1}^{N} \alpha_{yp} \frac{\partial Q_p(\mathbf{X}_0)}{\partial Y} \end{pmatrix} \tag{18}$$

Finally, interpolation is used again to obtain the displacement gradient, and thus the strains over the deformed grid $\mathbf{x}_k$ as

$$\nabla_{\mathbf{X}_0}\mathbf{u}_k(\mathbf{x}_k) = \nabla_{\mathbf{X}_0}\mathbf{u}_k(\mathbf{X}_0 + \mathbf{u}_k(\mathbf{X}_0)) \tag{19}$$

3.3 Thermal imaging post-treatment

The measurement of surface temperature as such is of limited interest since it has to be matched with the generated powers involved in the cutting phenomenon. Indeed, as pointed by many authors [36, 24] most of the generated heat is extracted along with the chip. It therefore affects the cutting force but only very remotely the generated surface. Accordingly, the thermal information is mostly intresting from an energy balance point of view and in order to investigate the tight couplings between constitutive equations and temperature. Let's recall the specific form of the heat diffusion equation in the Lagrangian configuration applied to a 2D thermographic framework (readers should refer to Appendix A for detail on the establishement of such relation and its related hypothesis).

$$\boldsymbol{\rho}\mathbf{C_p}\left(\frac{\partial \bar{\theta}}{\partial t} + \vec{v}\cdot\vec{\nabla}\bar{\theta}\right) - k_1\left(\vec{\nabla}\bar{\theta}\right)^2 - \mathbf{k}\Delta_2\bar{\theta} + \frac{2h\theta}{d} + \frac{2\sigma\epsilon}{d}(\bar{T}^4 - T_r^4) = w'_{ch} \tag{20}$$

where:

- $\bar{\theta} = \bar{T}(\mathbf{x},\mathbf{t}) - T_0$ is the difference between the current surface temperature field and the initial state where the temperature T_0 is assumed to be homogeneous and equal to the room temperature.
- $\boldsymbol{\rho}\mathbf{C_p}\left(\frac{\partial \bar{\theta}}{\partial t} + v\nabla\bar{\theta}\right)$ is the inertial term that reads the temperature evolution at a given location $(\mathbf{x},\mathbf{t})$. Variable v stands for the velocity vector field.
- $k_1\left(\vec{\nabla}\bar{\theta}\right)^2 - \mathbf{k}\Delta_2\bar{\theta}$ is the diffusion (Laplace's) term. Note that∇ is the two dimensionnal gradient and Δ_2 the two-dimensionnal Laplace operator.
- $\frac{2h\theta}{d} + \frac{2\sigma\epsilon}{d}(T^4 - T_r^4)$ is the convective and radiative heat losses over the front and back faces of the sample. σ here stands for the Stefan-Boltzman constant. h is the heat transfer coefficient arbitrary chosen to equal $50W.m^{-2}.K^{-1}$ (forced convection) and d is the depth of cut.

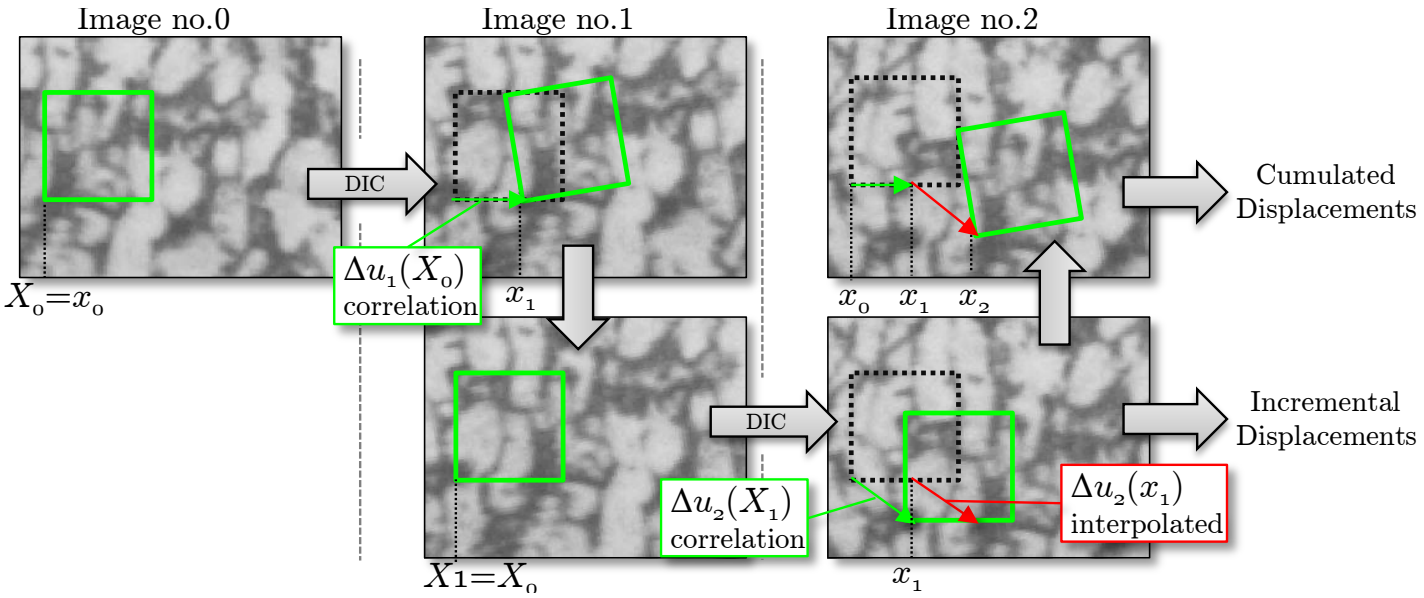

Figure 6: *Illustration of the computation scheme used to assess the cumulated displacement from incremental correlation.*

- $w'_{ch} = d_1$ is the heat source term and equals the intrinsic dissipation d_1 in absence of the thermoelastic couplings (see Appendix A).
- The material parameters are then $\boldsymbol{\rho} = \rho_1\theta + \rho_0$ the mass density, $\mathbf{C_p} = C_1\theta + C_0$ the specific heat, $\mathbf{k} = k_1\theta + k_0$ the thermal conductivity. The values and dependencies of these parameters to temperature are disscused in the above within the section 1.3.

The objective is here to compute the left hand side terms from the measured quantities ($\bar{T}(\mathbf{x}, \mathbf{t})$ and T_0) and the material parameters in order to provide an estimation of the involved power in the cutting phenomenon w'_{ch}. In practice, the computation of the Laplace operator over noisy data required the use of filtering. The chosen approach relies on the same projection used for strains (see Eq.17). In addition, the time derivative requires to evaluate the temperature in a Lagrangian framework while thermography provides it in Eulerian configuration. Hence, Motion Compensation Technique is used to retreive the material evolution of temperature from the fixed pixel evolution. Such approach is classical nowaday and is not detail any further here; readers can refer to [50, 46] for more details.

4 Results

4.1 Test at $V_c = 3m.min^{-1}$

The captured images consititues a film depicting the generation of 197 segments. Fig.8a presents 5 raw images of one single segment generation process (segment no.101). In addition it is worth mentionning that no drift of the thermomechanical quantities is observed during the cut. A total of 62 visible images and 6 thermal images are captured for this segment. For reading and comparison purpose, images are labelled by their number and the percentage of the segment formation. The first image (0%) being the image where the segment first touches the tool and the last image (100%) being the image exhibiting a displacement of $50\mu m$ after the segment being fully formed. It is seen from the raw images and Fig.8b that a crack continuously propagates along the primary shear band (denoted Z_I in the following). Fig.7a depicts the fluctuations of the cutting force. It can be seen that the cutting force peaks just prior the crack initiation (around 30%) and drops significantly when the crack reaches completion (about 60%). The magnitude of the force fluctuations equals 150 N meaning a tenth of the overall force. The average cutting force over the whole segment formation is $F_c = 1611$ N. The Fast Fourier Transform of the force signal provided in Fig.8b show a typical spectrum of a sum of two Gaussian distributions where the main peak matches the segmentation frequency (110 Hz) and the secondary correspond to the oscillations during the early stages of the segment generation (clearly visible in Fig.7a).

It can be seen from the strain depicted in Fig.8c that the three stages process described in [44] is clearly visible. The first two images (prior to 30% progression) show a diffuse deformation within the segment bulk, included in-between 0.3 and 0.8. Latter on, strains slowly converge to a localized zone ahead of the tool tip (clearly visible from 40%). Starting from this stage, strains accumulate in Z_I and lead to material failure. A crack propagates moving away from the tool tip. From image no.49 (80% and subsequent), the segment is fully formed and is extracted. It therefore undergoes rigid body motion and strains accumulation stops.

The strain rate field depicted in Fig.8d is of localized nature in the early stages of the process. Strains are accumlated at the same location all along the segment generation process. There is no clear evidence of any motion of the shearing zone conversly to previouly published results [35]. The primary shear zone model seems therefore particularly suited from these obsevations. Indeed, strain is generated by the fact that material particules are geometrically forced through this band and exit it with a strain that almost no longer evolves afterward (Fig.8c).

The temperatures imaging do not prompt any clear localisation within Z_I before 60% (i.e. the end of segment generation). The maximum temperature do not evolves significantly during the sequence, only ranging from 317°C to 360°C. However, the temperature gradient is significant in space. The min/max range within the same image roughly equals 300°C. Indeed, the main temperature rise seems to oc-

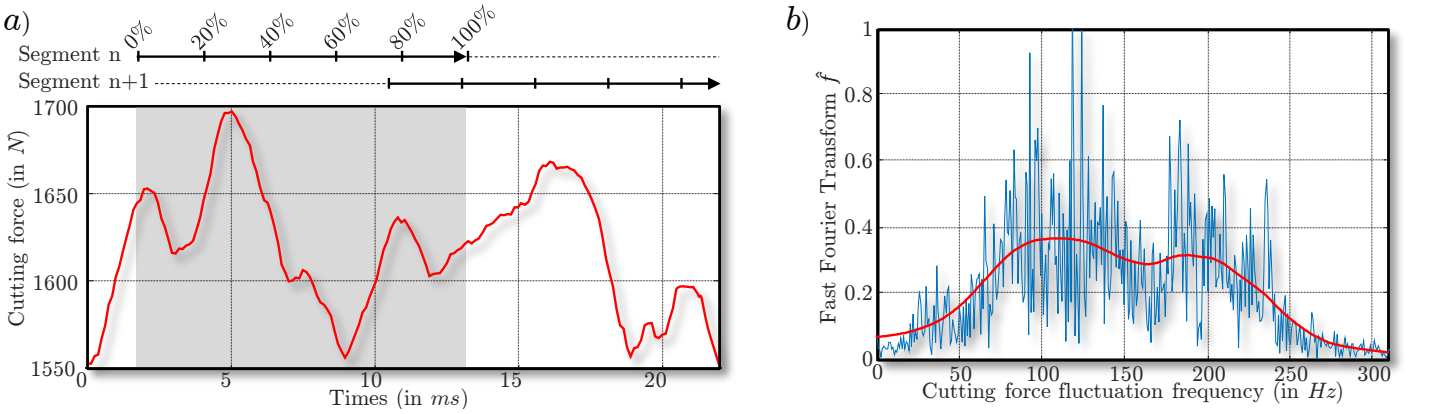

Figure 7: *a) Fluctuations of the cutting force over the generation of segment n0.101 and no.102 versus time. b) Fast Fourier Transform spectrum of the whoole force signal at* $V_c = 3m.min^{-1}$.

cur during the transit of a material point through the strain rate line (Z_I). It is also worth noticing that the maximum temperature location is not in the direct vicinity of the tool. Such consideration lead to consider that heat generated in Z_I (from plasticity and damage) prevails over the heat generated in the secondary and tertiary shear zone (due to friction over the rake or draft face).

Conversly to temperature, the computed heat source (Fig.8f) localizes during the early stage of segementation and almost simultaneously with the strains (depicted in Fig.8c). The dissipated power evolution also exhibits three stages: at fisrt, up to image no.6, the dissipated power is low (about $1.7 \times 10^{12}\ W.m^{-3}$) and is concentrated close to the tool. Then, from a progression in-between 20% to 60%, the dissipated power increases within Z_I from $2 \times 10^{12}\ W.m^{-3}$ to $3.2 \times 10^{12}\ W.m^{-3}$. The source also sligthly progress rightward (i.e. along the shear band from the tool tip to the free surface). Finally, it is seen from image no.49 (80%) that even while the crack propagation is completed, and that strain accumulation stalls, the generated power remains high and peaks around $3.2 \times 10^{12}\ W.m^{-3}$. It is also visible from the first image that when the generation of segment n starts the input mechanical power is split in two locations, the first consists in the sliding of the segment $n-1$ over the segment n and the second is the early stage of generating segment n. Indeed, it is clearly visible that a second source lights up beneath the sliding band and close to the tool tip.

4.2 Test at $V_c = 15m.min^{-1}$

At such cutting speed 248 segment are generated and with a frame rate of 6000 FPS the generation of a single segment last 11 images. Fig.9a depicts 5 images spread over the segment no.107 generation process. Comparatively, with a capture frequence of 600 FPS only one thermal image is acquired during the process and corresponds to a 40% progression. For this very reason, the other thermal images presented in Fig.9e are not otained from the investigated segment but from other measured segments but at the same stages of the segmentation progression. For this test, the average cutting force over the whole segment formation equals $F_c = 1516\ N$.

The crack progression differs from the one presented for a cutting speed of 3 $m.min^{-1}$ (Fig.8b). Indeed, the crack does not progess from 0% to 40% and suddenly propagates almost all the way to the free surface at image no.6 (60%). The pheneomon therefore seems to be more brutal at high cutting speed. This observation is confirmed by the investigation of the strain field depicted in Fig.9c. Eventhough these latter exhibit the same kind of diffused strain within the segment bulk (about 0.7), the shear localization within Z_I appears later (at 60% instead of 20% or 40%). It is also worth noticing that the total strain reached at 80% (i.e. at failure) is 1.5 which is lower than its counterpart at lower cutting speed (1.7).

The strain rates fields exhibit similar features regardless of the cutting speed. Their magnitude obviously increases with the cutting speed but in a linear manner. Indeed, one would expect that multiplying the cutting speed by 5 would increase the strain-rate magnitude by the same ratio, which is almost the case here. Hence, the difference of crack propagation nature is explained by the only fact that strain at failure decreases as the thermomechanical loadings increases.

As expected, the temperature rises higher as the cutting speed increases and reaches a maximum of $548°C$. It is also seen that the localization of the thermal fields is more obvious at such cutting speed even at the very early stages. In addition, it is observed that the maximum temperature decreases in the early stage of segment generation (between 10% and 20%) then increases again while the crack reaches completion. This could be explained by the fact that the heat source image at 10% actually reads two primary shear zones, the one at the tool tip (which leads to generate the observed segment) and another one, higher along the tool rake face, correponding to the previous segment.

From this perspective, the thermal dissipation fields depicted in Fig.9f are consistent with the observation made at 3 $m.min^{-1}$. Indeed, the heat source originates from the subsurface at the tool tip then spreads and moves rigthward along Z_I. It is also noticed that the dissipation band is narrower. The magnitude of the source however rises question since it appears to be only multiplied by a factor of roughly 3 while the cutting speed and the strain rate are increased by a factor of 5. This leads to conclude that segmentation in Z_I (where the heat source are higher) do not develops at iso-energy. In addition, it is worth noticing that the dissipation prompts at 80% has exactly the same shape and magnitude that image at 0% (not depicted in Fig9). This illustrates the cyclic nature machining under such conditions.

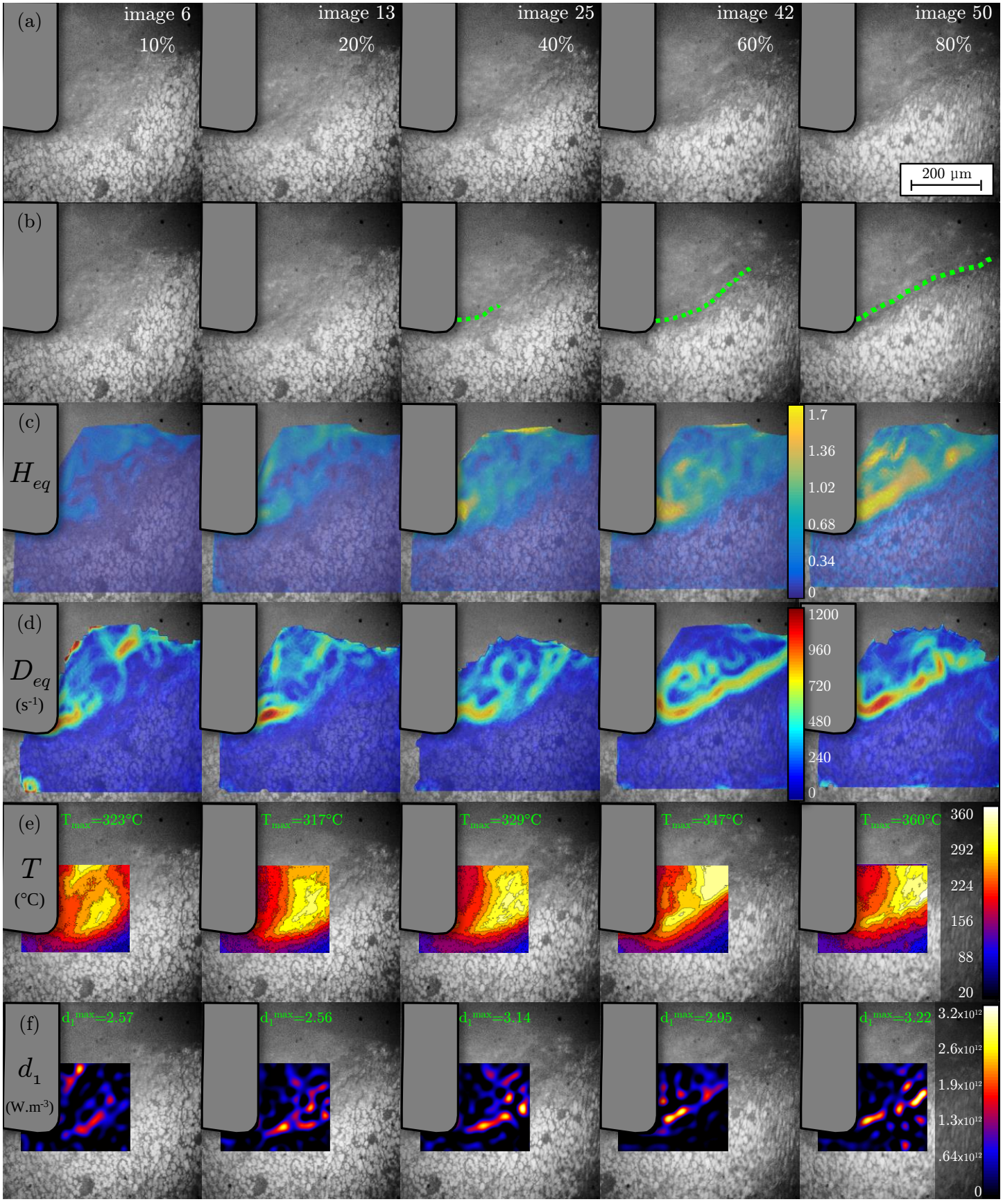

Figure 8: *a) Raw images of the chosen segment at* $3m.min^{-1}$*, images no.6, no.13, no.25, no.42 and no.50 (final image is no.62). b) Crack evolution along the primary shear zone. c) Logarithmic equivalent strain. d) Equivalent strain rate (in* s^{-1}*). e) Measured temperature (in* $°C$*). f) Intrinsic dissipation (specific mechanical power in* $W.m^{-3}$*).*

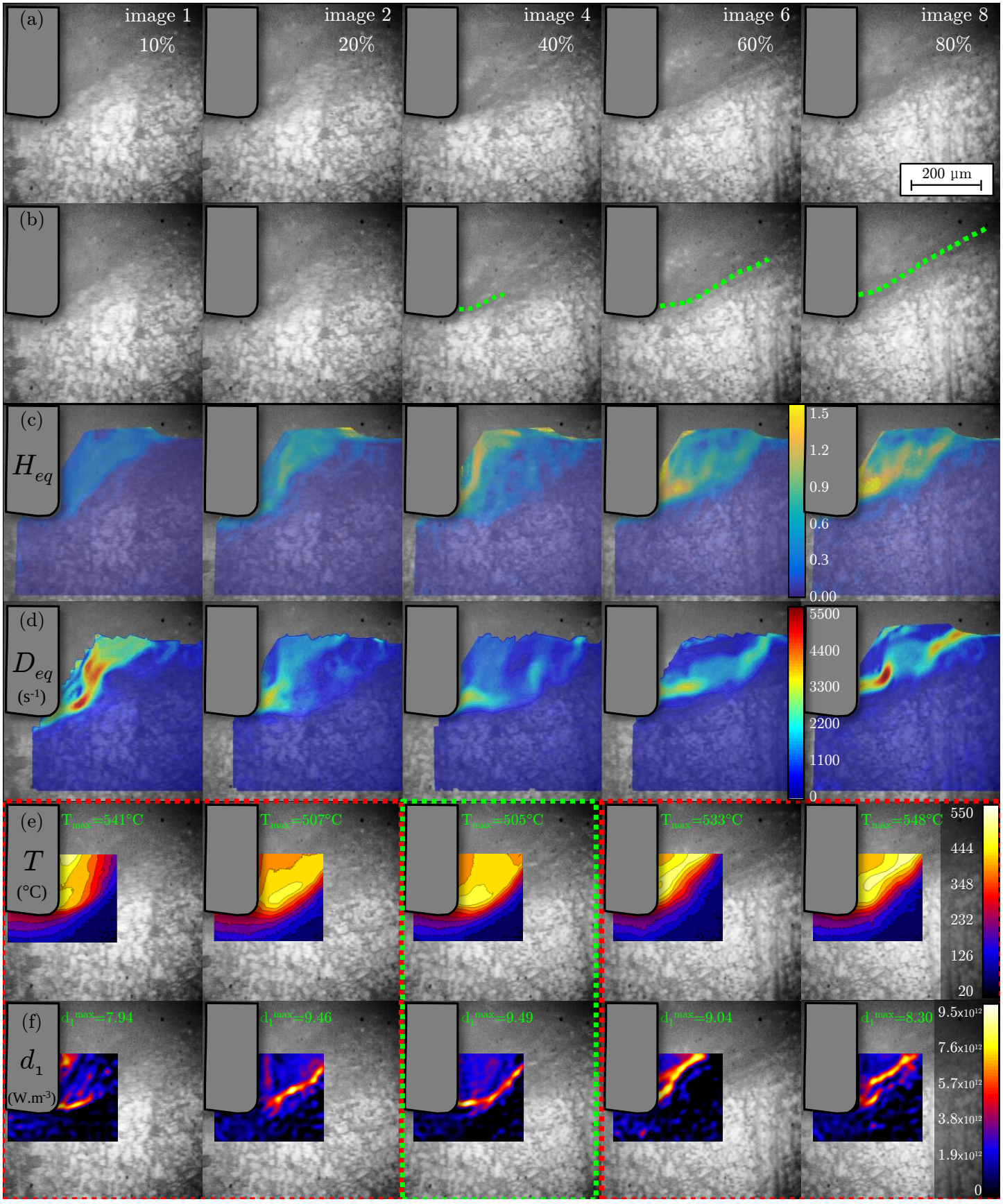

Figure 9: *a) Raw images of the chosen segment at* $15m.min^{-1}$*, images no.1, no.2, no.4, no.6 and no.8 (final image is no.10). b) Crack evolution along the primary shear zone. c) Logarithmic equivalent strain. d) Equivalent strain rate (in* s^{-1}*). e) Measured temperature (in* $°C$*). f) Intrinsic dissipation (specific mechanical power in* $W.m^{-3}$*).*

5 Discussion

The use of coupled measurement provides a valuable insight of serrated chips generation phenomenon from which some conclusions can be drawn but it also rises many subsequent questions. The present disscussion aims at summarizing and sorting the obtained information.

5.1 Force measurements

First, as seen from the heat source assessement, the generation of segment n partially overlap in time the generation of segments $n-1$ and $n+1$. This explains the difficulty in post-processing macroscopic measurment such as force measurements. Indeed, the variations of the force applied by a segment on the rake face cannot be measured from dynamometric measurements since the force applied by segment n sum up with the force applied by segment $n+1$ or $n-1$ [15]. It is also seen that the overall cutting force decreases as the cutting speed increases (from 1611 N down to 1516 N). This results is easily explained by the addition of thermal softening (significant between 300° and 550°C [14]) and the stick-slip nature of the friction phenomenon at low cutting speed [65].

5.2 Kinematic fields

Second, eventhough the strain fields are heterogeneous in space and in time, it seems that the strains always cumulate at the same location. As seen from strain rates field, the straining band is fixed in space and only fluctuates in magnitude over time. In addition, other tests performed with different rake angles (not presented here) suggest that the shape of the straining zone (its angle) is strongly related to the cutting geometry (feed and rake angle). This is clearly a perspective to the present work [25].

The equivalent strain at failure is smaller at high cutting speed eventhough the temperature in Z_I is higher. A first explanation for this phenomenon would be that the loss of ductility due to the viscous behaviour of metal overtakes the thermal softening in this range of thermo-mechanical loading. Another explanation would be related to the nature of the strain field itself. Indeed, as seen from the heat sources computations, the primary shear band narrows as strain rate increases which pleads for a strain path closer to pure shear than its counter-part at low cutting speed. This latter explanation seems to be confirmed by the detailed results presented in Fig.10 in which it is seen that at small cutting speed, the deformation in Z_I is a mix of shear and compression while at 15 $m.min^{-1}$, shear is clearly the main straining mode.

5.3 Thermal informations

From a thermal stand point, the maximum temperature is always observed within Z_I and away from the tool. One can therefore assumed that the temperature measured from a thermocouple positioned within the insert do not reads the proper temperature of Z_I. Consequently, it is hard to extrapolate from such measure the value of τ_f the shear friction stress and therefore the generated heat flux along Z_{II} commonly defined as [24]:

$$\dot{q} = \beta_{sl}\eta_f \cdot \tau_f \cdot V_{sl} \tag{21}$$

where V_{sl} is the sliding velocity and η_f the part of the frictional work converted into heat. β_{sl} is the ratio of the frictional power entering the material ($1-\beta_{sl}$ being the power ratio entering the tool). Indeed, the thermal softening of the material in Z_I is the leading factor of the stresses at tool/chip interface (i.e. Z_{II}) and a proper knowledge of temperature distribution in Z_I is therefore a key issue in assessing any energetic quantity in Z_{II}.

Although most of the heat ultimately ends up in chip, it is seen that the temperature spreads significantly beneath the tool (i.e. in the generated surface) for both cutting speeds. Further investigations are required to link this heat peak to the residual stresses distribution in the generated surface.

As expected, multiplying the cutting speed by five do not multiply the temperature variation ($\theta = T(\mathbf{x},\mathbf{t}) - T_0$) by five but only by 1.5 while the maximum dissipated power within Z_I (see Fig.8f and Fig.9f) is roughly multiplied by 3. This simple observation challenges the adiabaticity hypothesis often set within the three shear zones Z_i. If the dissipation is multiplied by 3, under adiabatic conditions, the temperature variation should by multiplied by 3 as well, which is not the case, meaning that the heat is somehow diffusing. Indeed, it is also observed that the second term (the so-called Laplace's term) of the heat diffusion equation Eq.(20), is clearly not negligible before the inertial term ($\rho C_p \dot{\theta}$) especially at small cutting speed. As seen in Fig.11, at $15 m.min^{-1}$, these two terms exhibits the same order of magnitude, eventhough the thermal conductivity of titanium allows is small.

5.4 Local Powers

From an energy stand point, it is also noticed in Fig.11, that the convective and radiative thermal losses on the side of the sample are negligible. It is also reasonnable to assume that even if extrapolated at higher cutting speeds (typ. $60 m.min^{-1}$) it remains negligible despite the presence of T^4. Alike the thermal losses, the variation of kinetic energy is small and will remain so, regardless of the cutting speed. Under such hypothesis and those exposed in Appendix A, the classical power balance becomes (local formulation):

$$\begin{aligned} w'_{ext} &= -w'_{int} + \dot{k} = w'_e + w'_a + \dot{k} \\ \Rightarrow w'_{ext} &\approx w'_a \end{aligned} \tag{22}$$

where w'_{ext} and w'_{int} are the external and internal specific power, w'_e and w'_a are the elastic and anelastic powers and $\dot{k}$ is the variation of kinetic energy.

Zone I: Heat is mainly generated within Z_I. Indeed, at both cutting speed, the dissipated powers at stake and the temperatures in Z_{II} and Z_{III} are significantly lower than in Z_I. However, plasticity may not, on it's own, be responsible for the observed dissipated power in Z_I. Indeed, recalling that Fig.8f and Fig.9f read the left hand side terms of Eq.(20) and assuming that plasticity is the only phenomenon involved in the thermal rise within Z_I, it classically comes that the specific dissipated power equals [16]:

$$w'_{ch} = \beta w'_a = \beta\left(\sigma : \dot{\epsilon}_p\right) \tag{23}$$

where β is the so-called Taylor-Quinney coefficient. Note that the thermo-elastic coupling is here neglected before plasticity [11]. Hence, assuming a constant value of β of 0.8 ([38]), it comes that the maximal value of the equivalent Von-Mises stresses roughly equal 2.1 GPa for the test at 15 $m.min^{-1}$ and

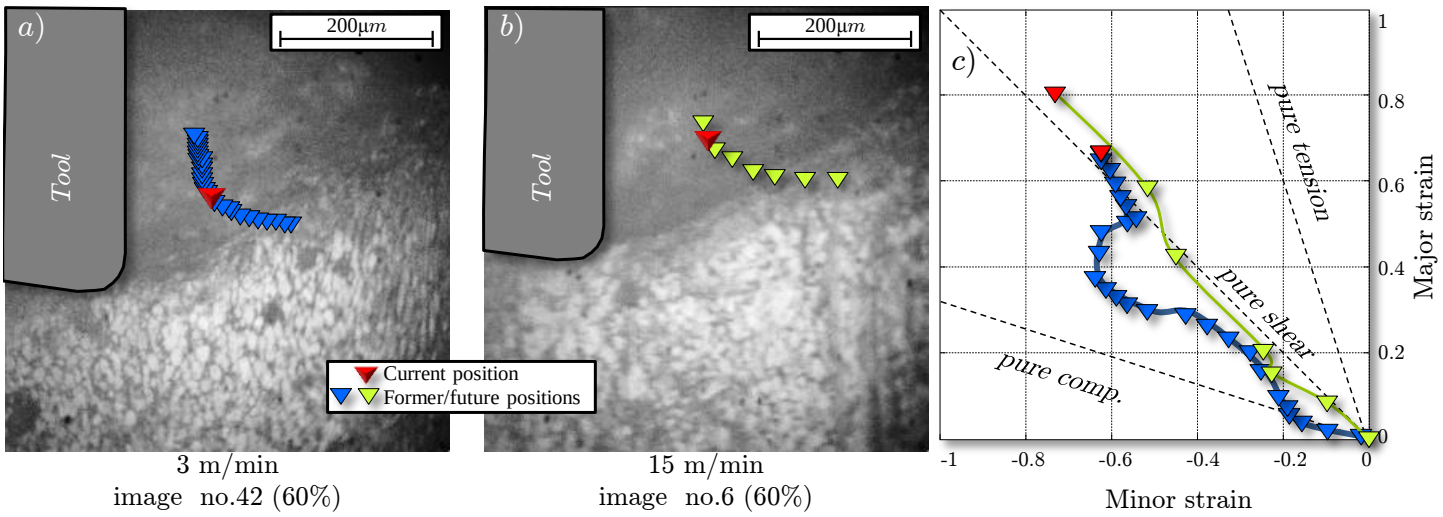

Figure 10: *a) Trajectory of the considered point, up to material failure, for the test at 3 $m.min^{-1}$. b) Trajectory of the considered point, up to material failure for the test at 15 $m.min^{-1}$. c) Strain path up to failure for both considered points (cutting speed) in the strain principal plane.*

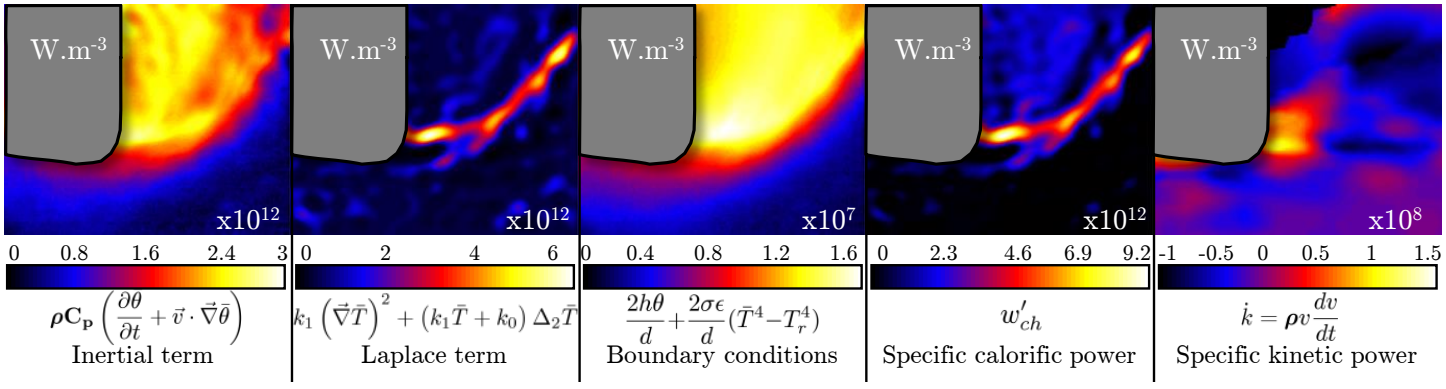

Figure 11: *Shares of power contribution for the test at 15$m.min^{-1}$ (progression 40%) unit is $W.m^{-3}$. a) Inertial term. b) Diffusive (Laplace) term. c)boundary condtion term. d) Intrinsic dissipation. e) Kinetic term.*

3.3 GPa for the test at 3 $m.min^{-1}$ which seems largly overestimated. Such calculation is, of course, too coarse but lead to consider that, especially at small cutting speed, other phenomenon are involved (damage, segment-over-segment friction, phase transition, recrystalization...) and that other dissipative terms should be padded to the right hand side of Eq.(22).

Zones II and III : The presented measurements mainly focused on the primary shear zone. Nonetheless they provide valuable information on other dissipatives zones (namely Z_{II} and Z_{III}). Indeed, from the thermal information it is possible to assess the heat flux transfering between the tool and the material. The Neumann boundary condition provides the incoming surface heat flux which can be compared to Eq.(21) as:

$$\dot{q} = -\mathbf{k}\frac{\partial\theta}{\partial x} = \beta_{sl}\eta_f \cdot \tau_f \cdot V_{sl} - h(T_w - T_{tool}) \qquad (24)$$

Hence, evaluating the temperature gradient over the material frontier $\partial\Omega$ provides the heat fluxes depicted in Fig.12 for both Z_{II} and Z_{III}. It can be seen that the power generated by friction in Z_{II} is not sufficient to overcome the natural flux heading from the hot segment toward the tool (cooler). It is also seen that increasing the cutting speed slightly increases the outbound heat flux. However, this increase is not proportional to the cutting speed and is to be matched with the tool temperature (see Eq.(24)). Regarding Eq.(24), it can be concluded that in Z_{II}, the current tool temperature T_{tool} is of the utmost importance for whoever wants to relate tool wear to the incoming thermal flux. Indeed, if T_{tool} is no longer an unknown variable, a given set of parameters β_{sl}, η_f and h leads to a possible assessement of the last unknown variable: τ_f a key variable in machining operations.

In Z_{III} heat is entering the material, meaning that the generated surface is hot and slowly diffuses within the material. It is seen that the cutting speed strongly affects the surface temperature beneath the tool which doubles between 3 $m.min^{-1}$ and 15 $m.min^{-1}$ (approximatively 140°C and 300°C). This ratio of 2 is also observed between the heat flux in Z_{III} depicted in Fig.12. No discontinuity is observed in the incoming flux which leads to consider that there is no contact between the tool and the part along the clearance face.

5.5 Global Powers

From a global stand point, it is worth recalling that the overall input power of the cut is the cross product of the cutting force with the cutting speed and that the internal energy balance alows to write that:

$$W'_{ext} = F_c \cdot V_c = -W'_{int} + \dot{K} = W'_e + W'_a + \dot{K} \qquad (25)$$

where $\dot{K}$ is the variation of kinetic energy, W'_{int} is the internal power, W'_e the elastic power, W'_a the anelastic power, all being expressed in $Watts$. Hence, by neglecting the elastic power and $\dot{K}$ before the anelastic power, it is possible to evaluate the part of energy consumed in each of the three zones from the spatial intergation of the specific dissipation $w'_{ch} = \beta w'_a$ depicted in Fig.8f and Fig.9f. It therefore comes:

$$W'_{ext} = \frac{d}{\beta}\int_{\bigcup_{i=I}^{IV} Z_i} w'_{ch} dS \qquad (26)$$

where d is the depth of cut, Z_i is the surface area of the zones Z_I, Z_{II} and Z_{III} and Z_{IV} is the remaining surface corresponding to the imaged sub-surface of the sample and the bulk of the chip segment as depicted in Fig.13. The volume integration is performed under the strong assumption that the heat source is of homogeneous nature along the depth of the sample. Finally, dividing this quantity by the cutting speed results in obtaining $\tilde{W}_{ext}$ expressed in $J.m^{-1}$; the energy required to perform 1 meter of cut. Fig.13 depicts for the 5 instants of each tests, the shares of energy consumed by each of the three zones (Z_I, Z_{II}, Z_{III}) and in the rest of the imaged area Z_{IV} (denoted bulk & sub-surface in Fig.13). Various considerations can be made from such representation:

- As expected from the force measurements interpretation, the overall consumed energy decreases as the cutting speed increases (which is consistant with classical dynamometric observation).
- The dissipation in the segment bulk and in the subsurface (i.e. outside of the three indentified and well known shear zones) is far from negligible. It is consistent with the strains measurments presented in the above where it is seen that smaller but significant deformation occurs within the bulk of the segment.
- The dissipation in the segment bulk suddenly drops when the crack propagation reaches completion (see Fig.13 progression 60% for both tests).
- The energy dissipated through plasticity in the subsurface of Z_{II} and Z_{III} slightly increases with the cutting speed, especially for Z_{III}. The interpretation of (Eq.23) leads to assume that the plastic deformation in these zones also increases with the cutting speed.
- For most of the investigated instants, the internal energy comes close to the external one. Meaning that most of the energy is used within the captured area. However, a part of the input energy is consumed outside of the image. Further investigations would be required to sort out if this energy is used to deform the subsurface (left of Z_{III}) or the top section of Z_I both unseen from the imaging apparatus.

Conclusions and Perspectives

In this paper, the development and the implementation of an original imaging apparatus dedicated to the simultaneous measurement of strain and temperature fields at small scale is presented. The proposed experiment enables the monitoring of a $500 \times 500\mu m$ area at the tool tip using both visible and infrared cameras. The study provides a novel and valuable insight to essential thermomechanical couplings and in-process mechanical phenomena involved in the generation of serrated chips and thus gives a new understanding of essential cutting process mechanics occurring during the orthogonal cutting of Ti-6Al-4V. The developed numerical post-processing also constitutes an original contribution since it provides fields information at various time steps of the serrated chip generation progression. Strain, strain-rates, temperatures, dissipated powers along with displacement, velocity and crack progression are obtained at each pixel from both kinematic and thermal/energy measurement. It allows the assessment

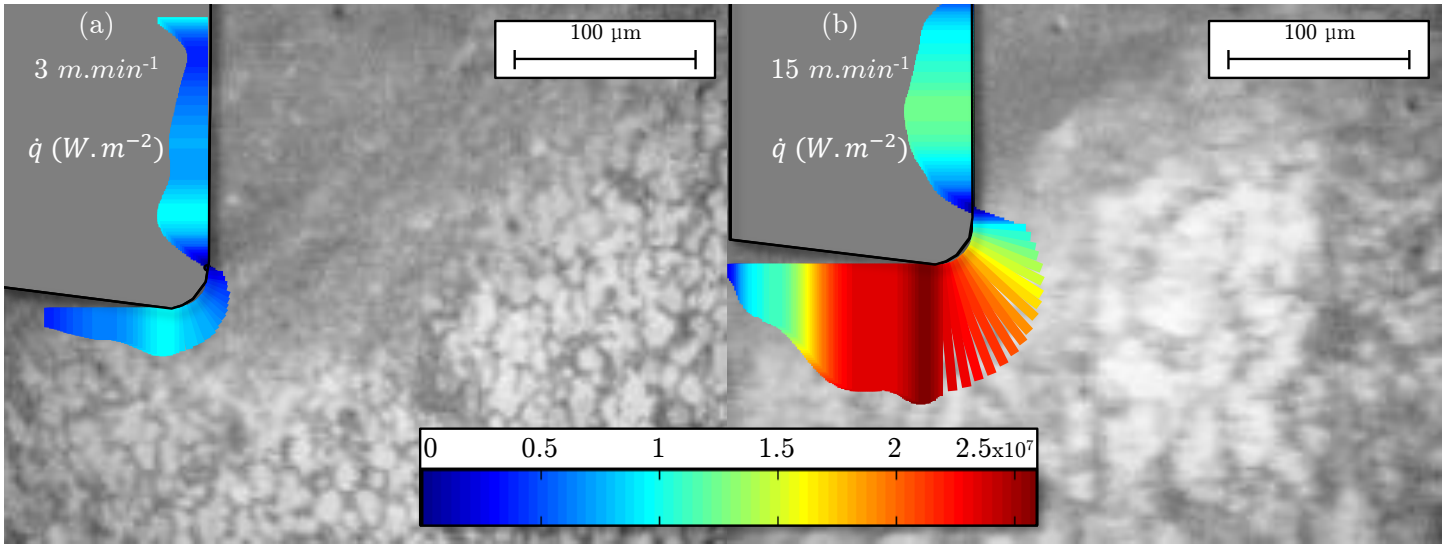

Figure 12: *Averages heat flux entering/exiting the material from the tool/part interfaces of Z_{II} and Z_{III} during one segment generation. a) at 3 $m.min^{-1}$. b) at 15 $m.min^{-1}$*

of the dissipated powers at stake during material removing processes. The whole measuring chain has been strongly calibrated and a special attention has been paid to the dependency of the physical parameters to temperature.

The experimental observations have highlighted the dependency of the physical phenomena to the cutting speed. This work provides valuable experimental evidences on the different nature of the coupling phenomenon. First, it appears that the nature of the deformation mechanisms is clearly affected by the cutting speed, in terms of magnitude but also in term of strain path. At low cutting speed, the loading in the primary shear zone is a mix of shear and compression, while it becomes mainly pure shear at higher cutting speed. Also, the width of the primary shear zone decreases as the cutting speed increases. It has been confirmed that the heat is mainly generated in the primary shear zone, and the highest temperature is observed in this zone and not along the rake face interface. In addition, the energetic study conducted in this work demonstrated that the adiabaticity hypothesis often set within the three shear zones is disputed. Indeed, as the dissipation is multiplied by 3, the temperature variation is not multiplied by 3 as well, meaning that the heat is somehow diffusing. It is also observed that the Laplace's term of the heat diffusion equation is clearly not negligible before the inertial term, especially at small cutting speed. Moreover, plasticity is not the only responsible for the dissipated power in the primary shear zone. Other phenomena may be involved (damage, segment-over-segment friction, phase transition, recrystallization...). The study also showed that a significant power is dissipated outside the three shear zones and mostly within the segment bulk.

Moreover, even though the heat is mainly evacuated within the chip, the generated surface temperature evolution is significant and this surface is most probably thermally affected. This constitutes a direct perspective of this work. A proper knowledge of temperature distribution in this zone is a key issue in assessing any energetic quantity in the chip, in the material and at the tool/chip interface. Especially, acquiring detailed coupled measurements in Z_{II} and Z_{III} would be of high interest in order to improve understanding of tool wear and of the thermal influence on the fatigue behavior of the generated surface.

Appendix A

Let's assume a thermal dependance of the physical constants: thermal conductivity, mass density and specific heat as

$$\begin{cases} \mathbf{k} = k(\theta) = k_1\theta(\mathbf{x},t) + k_0 \\ \boldsymbol{\rho} = \rho(\theta) = \rho_1\theta(\mathbf{x},t) + \rho_0 \\ \mathbf{C_p} = C_p(\theta) = C_1\theta(\mathbf{x},t) + C_0 \end{cases} \tag{27}$$

where k_1 is the first term of the linear regression from the data presented in Tab.1 and k_0 the thermal conductivity at $20°C$ (idem for the ρ_i and C_i). $\theta = T(\mathbf{x},t) - T_0(\mathbf{x})$ is the temperature variation to the initial temperature T_0 The heat diffusion equation with variable conductivity, mass density and specific heat is:

$$\boldsymbol{\rho}\mathbf{C_p}\frac{d\theta}{dt} - \vec{\nabla}\left(\mathbf{k}\vec{\nabla}\theta\right) = w'_{ch} + r_\epsilon(\theta) \tag{28}$$

where w'_{ch} is the specific calorific power (i.e. the internal heat source).The thermoealstic coupling are here neglected since the plastic strains largely prevail over the elastic ones. Readers can refer to [11] and [48] for more details. Another hypothsesis assumed here is that r_ϵ, the volume external radiative sources do not depend on temperature T. It comes that $r_\epsilon(T) = r_\epsilon(T_0)$ and therefore that $r_\epsilon(\theta) = 0$.

Using the Kirshoff transform of the temperature:

$$\Psi(T) = \int_0^\theta k(\theta')d\theta' \tag{29}$$

and its two subsequent relations

$$\frac{d\Psi}{dt} = \mathbf{k}\frac{d\theta}{dt} \quad \text{and} \quad \vec{\nabla}\Psi = \mathbf{k}\vec{\nabla}\theta \tag{30}$$

the heat diffusion equation Eq.(28) becomes:

$$\underbrace{\frac{\boldsymbol{\rho}\mathbf{C_p}}{\mathbf{k}}\frac{d\Psi}{dt}}_{\mathcal{I}(\Psi)} - \underbrace{\vec{\nabla}\left(\vec{\nabla}\Psi\right)}_{\mathcal{D}(\Psi)} = w'_{ch} \tag{31}$$

where the left hand side term $\mathcal{I}(\Psi)$ is called the inertial term and the right one $\mathcal{D}(\Psi)$ is called diffusive term.

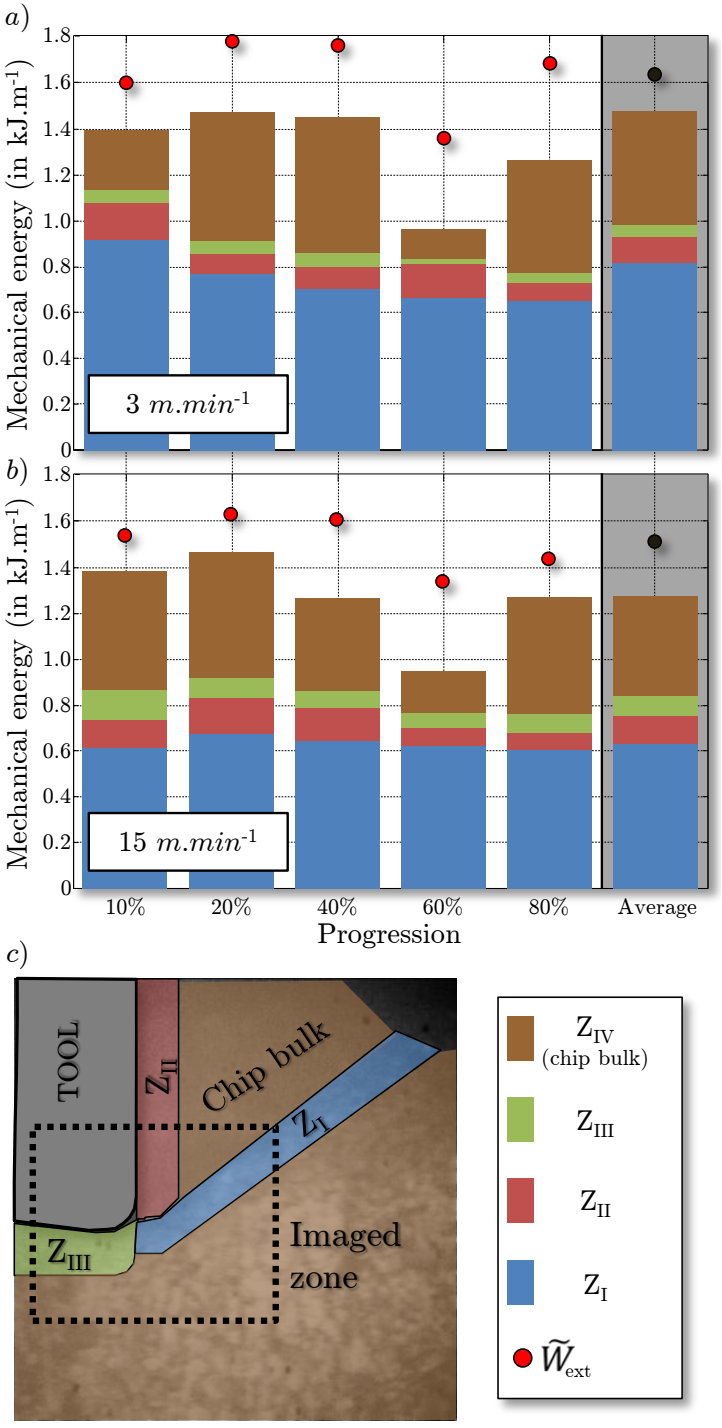

Figure 13: *Shares of energy consumed per zone of the image (red dot stand for the external energy $\tilde{W}_{ext}$).a) at 3 $m.min^{-1}$ and b) at 15 $m.min^{-1}$ c) Zones location and legend*

The key point here is that the available experimental data do not read the third dimension of the temperature fileds (along z). Indeed the thermal information is of surface nature and therefore requires to integrate the relation Eq.(31) over the z direction (through-thickness dimension). for this purpose the through thickness average of fields varaibles must be defined as:

$$\bar{\bullet} = \frac{1}{d}\int_0^d \bullet dz \tag{32}$$

where d is the thickness of the sample (i.e. the depth of cut). This imposes the set two main hypothesis [16]:

i) The calorific power w'_{ch} is constant through thickness : $\bar{w'}_{ch} = w'_{ch}$

ii) The heat conduction is much greater than the thermal losses (radiative and convective) of the front and back faces. It therefore comes that the averaged temperature through thickness can be approximated by the measured surface temperature $\bar{\theta} \approx \theta(z=0) \approx \theta(z=d)$.

the integrated diffusive term then becomes:

$$\begin{aligned}\bar{\mathcal{D}} &= \frac{1}{d}\int_0^d \left(\frac{\partial^2\Psi}{\partial x^2} + \frac{\partial^2\Psi}{\partial y^2} + \frac{\partial^2\Psi}{\partial z^2}\right) dz \\ &= \frac{1}{d}\frac{\partial^2}{\partial x^2}\int_0^d \Psi dz + \frac{1}{d}\frac{\partial^2}{\partial y^2}\int_0^d \Psi dz + \frac{1}{d}\left[\frac{\partial\Psi}{\partial z}\right]_0^d \\ &= \left[\frac{\partial^2\bar{\Psi}}{\partial x^2} + \frac{\partial^2\bar{\Psi}}{\partial y^2}\right] + \frac{1}{d}\left[\mathbf{k}\frac{\partial\theta}{\partial z}\right]_0^d \\ &= \Delta_2\bar{\Psi} + \frac{1}{d}\left[\mathbf{k}\frac{\partial\theta}{\partial z}\right]_0^d\end{aligned} \tag{33}$$

where Δ_2 is the two-dimensional Laplace operator such as

$$\begin{aligned}\Delta_2\bar{\Psi} &= \vec{\nabla}\cdot\left(\vec{\nabla}\bar{\Psi}\right) \\ &= \vec{\nabla}\cdot\left(k(\bar{\theta})\vec{\nabla}\bar{\theta}\right) \\ &= \vec{\nabla}\cdot\left(k_1\bar{\theta}\vec{\nabla}\bar{\theta} + k_0\vec{\nabla}\bar{\theta}\right) \\ &= k_1\vec{\nabla}\cdot\bar{\theta}\vec{\nabla}\bar{\theta} + k_0\vec{\nabla}\cdot\vec{\nabla}\bar{\theta} \\ &= k_1\left(\vec{\nabla}\bar{\theta}\cdot\vec{\nabla}\bar{\theta} + \vec{\nabla}\cdot\vec{\nabla}\bar{\theta}\times\bar{\theta}\right) + k_0\Delta_2\bar{\theta} \\ &= k_1\left(\vec{\nabla}\bar{\theta}^2 + \Delta\bar{\theta}\times\bar{\theta}\right) + k_0\Delta_2\bar{\theta} \\ &= k_1\left(\vec{\nabla}\bar{\theta}\right)^2 + \mathbf{k}\Delta_2\bar{\theta}\end{aligned} \tag{34}$$

and ∇ is here the two-dimensional gradient. The integrated inertial term $\bar{\mathcal{I}}$ is expressed through the partial derivative of Ψ and the Liebniz intergration rule as:

$$\begin{aligned}\bar{\mathcal{I}} &= \frac{1}{d}\int_0^d \frac{\boldsymbol{\rho}\mathbf{C_p}}{\mathbf{k}}\frac{d\Psi}{dt}dz \\ &= \frac{\boldsymbol{\rho}\mathbf{C_p}}{\mathbf{k}d}\frac{d}{dt}\int_0^d \Psi dz \\ &= \frac{\boldsymbol{\rho}\mathbf{C_p}}{\mathbf{k}}\frac{d\bar{\Psi}}{dt} \\ &= \boldsymbol{\rho}\mathbf{C_p}\frac{d\bar{\theta}}{dt} \\ &= \boldsymbol{\rho}\mathbf{C_p}\left(\frac{\partial\bar{\theta}}{\partial t} + \vec{v}\cdot\vec{\nabla}\bar{\theta}\right)\end{aligned} \tag{35}$$

where $\vec{v} = \vec{v}(\mathbf{x}, t)$ is the 2D velocity vector field. Finally, it should be noticed that the right hand side term of eq.(33) reads the boundary condition of the front and back faces of the sample. Therefore, assuming a convective/radiative conditions on these faces and an room temperature denoted T_r that equals the intitial temperature T_0, one can write that:

$$-\left[\mathbf{k}\frac{\partial\theta}{\partial z}\right]_0^d = 2h\bar{\theta} + 2\sigma\epsilon(\bar{T}^4 - T_r^4) \tag{36}$$

and the completed heat diffusion of the problem at instant t can be expressed as:

$$\boxed{\boldsymbol{\rho}\mathbf{C_p}\left(\frac{\partial\bar{\theta}}{\partial t} + \vec{v}\cdot\vec{\nabla}\bar{\theta}\right) - k_1\left(\vec{\nabla}\bar{\theta}\right)^2 - \mathbf{k}\Delta_2\bar{\theta} + \frac{2h\theta}{d} + \ldots \frac{2\sigma\epsilon}{d}(\bar{T}^4 - T_r^4) = w'_{ch}} \tag{37}$$

Remark: under such formalism, the use of a Stefan-Boltzmann condition imposes to express the tempratures T and $T_r = T_0$ in Kelvin (and not in Celsius)

References

[1] Abaqus, Inc. *ABAQUS Theory guide : version 6.12-1.* Providence, RI, USA : ABAQUS, 2016.

[2] J.P. Arrazola, I. Arriola, and M.A. Davies. Analysis of the influence of tool type, coatings, and machinability on the thermal fields in orthogonal machining of AISI 4140 steels. *CIRP Annals - Manufacturing Technology*, 58:85–88, 2009.

[3] P.J. Arrazola, I. Arriola, M.A. Davies, A.L. Cooke, and B.S. Dutterer. The effect of machinability on thermal fields in orthogonal cutting of aisi 4140 steel. *CIRP Annals - Manufacturing Technology*, 57:65–68, 2008.

[4] I. Arriola, E. Whitenton, J. Heigel, and P.J. Arrazola. Relationship between machinability index and in-process parameters during orthogonal cutting of steels. *CIRP Annals - Manufacturing Technology*, 60:93–96, 2011.

[5] J. Artozoul, C. Lescalier, O. Bomont, and D. Dudzinski. Extended infrared thermography applied to orthogonal cutting. *Applied Thermal Engineering*, 64:441–452, 2014.

[6] T. Baizeau, S. Campocasso, G. Fromentin, F. Rossi, and G. Poulachon. Effect of rake angle on strain field during orthogonal cutting of hardened steel with c-bn tools. *Procedia CIRP*, 31:166–171, 2015.

[7] D. Basak, R.A. Overfelt, and D. Wang. Measurement of specific heat capacity and electrical resistivity of industrial alloys using pulse heating techniques. *International Journal of Thermophysics, Vol. 24, No. 6, November 2003*, 24(6):1721–1733, 2003.

[8] L. Bodelot, E. Charkaluk, L. Sabatier, and P. Dufrénoy. Experimental study of heterogeneities in strain and temperature fields at the microstructural level of polycrystalline metals through fully-coupled full-field measurements by digital image correlation and infrared thermography. *Mechanics of Materials*, 43(11):654 – 670, 2011.

[9] M. Boivineau, C. Cagran, D. Doytier, V. Eyraud, M. H. Nadal, B. Wilthan, and G. Pottlacher. Thermophysical properties of solid and liquid ti-6al-4v (ta6v) alloy. *International Journal of Thermophysics*, 27(2):507–529, 2006.

[10] M. Bornert, F. Brémand, P. Doumalin, M. Dupré, J-C. Fazzini, M. Grédiac, F. Hild, S. Mistou, J. Molimard, J-J. Orteu, L. Robert, Y. Surrel, P Vacher, and B. Wattrisse. Assessment of digital image correlation measurement errors: Methodology and results. *Experimental Mechanics*, 49:353–370, 2008.

[11] T. Boulanger, A. Chrysochoos, C. Mabru, and A. Galtier. Calorimetric analysis of dissipative and thermoelastic effects associated with the fatigue behavior of steels. *International Journal of Fatigue*, 26:221–229, 2004.

[12] J. Buda. New methods in the study of plastic deformation in the cutting zone. *CIRP Annals*, 21:17–18, 1972.

[13] S.L. Cai, Y. Chen, G.G. Ye, M.Q. Jiang, Wang H.Y., and L.H. Dai. Characterization of the deformation field in large-strain extrusion machining. *Journal of Materials Processing Technology*, 216:48–58, 2015.

[14] M. Calamaz, D. Coupard, and F. Girot. A new material model for 2d numerical simulation of serrated chip formation when machining titanium alloy ti-6al-4v. *International Journal of Machine Tools and Manufacture*, 48(3-4):275–288, 2008.

[15] M. Calamaz, D. Coupard, and F. Girot. Strain field measurement in orthogonal machining of a titanium alloy. *Advanced Materials Research*, 498:237–242, 2012.

[16] A. Chrysochoos and H. Louche. An infrared image processing to analyse the calorific effects accompanying strain localisation. *International Journal of Engineering Science*, 38:1759–1788, 2000.

[17] C. Courbon, T. Mabrouki, J. Rech, D. Mazuyer, F. Perrard, and E. D'Eramo. Further insight into the chip formation of ferritic-pearlitic steels: Microstructural evolutions and associated thermo-mechanical loadings. *International Journal of Machine Tools & Manufacture*, 77:34–46, 2014.

[18] M.A. Davies, A.L. Cooke, and E.R. Larsen. High bandwidth thermal microscopy of machining. *CIRP Annals - Manufacturing Technology*, 54(1):63–66, 2005.

[19] E.P. Gnanamanickam, S. Lee, J.P. Sullivan, and S. Chandrasekar. Direct measurement of large-strain deformation fields by particle tracking. *Measurement science and technology*, 20:095710 (12p), 2009.

[20] L. González-Fernández, E. Risueño, R.B. Pérez-Sáez, and M.J Tello. Infrared normal spectral emissivity of ti-6al-4v alloy in the 500 - 1150 k temperature range. *Journal of Alloys and Compounds*, 541:144–149, 2012.

[21] A. Guery, F. Hild, F. Latourte, and S. Roux. Slip activities in polycrystals determined by coupling dic measurements with crystal plasticity calculations. *International Journal of Plasticity*, 81:249–266, 2016.

[22] Y. Guo, M. Efe, W. Moscoso, D. Sagapuram, K.P. Trumble, and S. Chandrasekar. Deformation field in large-strain extrusion machining and implications for deformation processing. *Scripta Materialia*, 66:235–238, 2012.

[23] Y. Guo, C. Saldana, W.D. Compton, and S. Chandrasekar. Controlling deformation and microstructure on machined surfaces. *Acta Materialia*, 59:4538–4547, 2011.

[24] B. Haddag, S. Atlati, M. Nouari, and M. Zenasni. Analysis of the heat transfer at the tool-workpiece interface in machining: determination of heat generation and heat transfer coefficients. *Heat Mass Transfer*, 51:1355–1370, 2015.

[25] M. Harzallah, T. Pottier, J. Senatore, M. Mousseigne, G. Germain, and L. Landon. Numerical and experimental investigations of ti-6al-4v chip generation and thermo-mechanical couplings in orthogonal cutting. *International Journal of Mechanical Sciences*, 134(Supplement C):189 – 202, 2017.

[26] J.C. Heigel, E. Whitenton, B. Lane, M.A. Donmez, V. Madhavan, and W. Moscoso-Kingsley. Infrared measurement of the temperature at the tool-chip interface while machining ti-6al-4v. *Journal of Materials Processing Technology*, 243:123–130, 2017.

[27] E. Héripré, M. Dexet, J. Crépin, L. Gélébart, A. Roos, M. Bornert, and D. Caldemaison. Coupling between experimental measurements and polycrystal finite element calculations for micromechanical study of metallic materials. *International Journal of Plasticity*, 23:1512–1539, 2007.

[28] A. Hijazi and V. Madhavan. A novel ultra-high speed camera for digital image processing applications. *Measurement Science and Technology*, 19(8):1–11, 2008.

[29] A. Içöz, L. Patriarca, M. Filippini, and Beretta S. Strain accumulation in tial intermetallics via high-resolution digital image correlation (dic). *Procedia Engineering*, 74:443–448, 2014.

[30] S.P.F. Jaspers and J. Dautzenberg. Material behaviour in metal cutting: Strains, strain rates and temperatures in chip formation. *Journal of Materials Processing Technology*, 121:123–135, 2002.

[31] Andrew Justice, Ibrahim Emre Gunduz, and Steven F. Son. Microscopic two-color infrared imaging of nial reactive particles and pellets. *Thin Solid Films*, 2016. The 43rd International Conference on Metallurgical Coatings and Thin Films.

[32] R.V. Kazban, K.M. Vernaza Peña, and J.J. Mason. Measurements of forces and temperature fields in high-speed machining. *Experimental Mechanics*, 48(3):307–317, 2008.

[33] F. Klocke, D. Lung, S. Buchkremer, and I. S. Jawahir. From orthogonal cutting experiments towards easy-to-implement and accurate flow stress data. *Materials and Manufacturing Processes*, 28(11):1222–1227, 2013.

[34] R. Komanduri and R.H. Brown. On the mechanics of chip segmentation in machining. *Journal of engineering for industry*, 103:33–51, 1981.

[35] R. Komanduri, T. Schroeder, J. Harza, B. Turkovich, and D. Flom. On the catastrophic shear instability in high-speed machining of an aisi 4340 steel. *J. Eng. Ind.*, 104:121–131, 1982.

[36] F. Kone, Czarnota C., B. Haddag, and M. Nouari. Finite element modelling of the thermo-mechanical behavior of coatings under extreme contact loading in dry machining. *Surface & Coatings Technology*, 205:3559–3566, 2011.

[37] T. Mabrouki and J.-F. Rigal. A contribution to a qualitative understanding of thermo-mechanical effects during chip formation in hard turning. *Journal of Materials Processing Technology*, 176:214–221, 2006.

[38] J.J. Mason, A.J. Rosakis, and G. Ravichandran. On the strain and strain rate dependence of the fraction of plastic work converted into heat: an experimental study using high speed infrared detectors and the kolsky bar. *Mechanics of Materials*, 17:135–145, 1994.

[39] B. Pan, Z. Lu, and H. Xie. Mean intensity gradient: An effective global parameter for quality assessment of the speckle patterns used in digital image correlation. *Optics and Lasers in Engineering*, 48:469–477, 2010.

[40] B. Pan, H. Xie, Z. Wang, K. Qian, and Z. Wang. Study on subset size selection in digital image correlation for speckle patterns. *Optics express*, 16:7037–7048, 2008.

[41] Bing Pan, Wu Dafang, and Xia Yong. Incremental calculation for large deformation measurement using reliability-guided digital image correlation. *Optics and Lasers in Engineering*, 50:586–592, 2012.

[42] A. Perrier, F. Touchard, L. Chocinski-Arnault, and D. Mellier. Mechanical behaviour analysis of the interface in single hemp yarn composites: Dic measurements and fem calculations. *Polymer Testing*, 52:1–8, 2016.

[43] J.-E. Pierré, J.-C. Passieux, J.-N. Périé, F. Bugarin, and L. Robert. Unstructured finite element-based digital image correlation with enhanced management of quadrature and lens distortions. *Optics and Lasers in Engineering*, 77:44 – 53, 2016.

[44] T. Pottier, G. Germain, M. Calamaz, A. Morel, and D. Coupard. Sub-millimeter measurement of finite strains at cutting tool tip vicinity. *Experimental Mechanics*, 54(6)(6):1031–1042., 2014.

[45] T. Pottier, H. Louche, S. Samper, H. Favreliére, F. Toussaint, and P. Vacher. Proposition of a modal filtering method to enhance heat source computation within heterogeneous thermomechanical problems. *International Journal of Engineering Science*, 81:163–176, 2014.

[46] T. Pottier, M-P. Moutrille, J-B. Le-Cam, X. Balandraud, and M. Grédiac. Study on the use of motion compensation techniques to determine heat sources. Application to large deformations on cracked rubber specimens. *Experimental Mechanics*, 49:561–574, 2009.

[47] N. Ranc, V. Pina, G. Sutter, and S. Philippon. Temperature measurement by visible pyrometry: Orthogonal cutting application. *J. Heat Transfer*, 126(6):931–936, 2003.

[48] D. Rittel. On the conversion of plastic work to heat during high strain rate deformation of glassy polymers. *Mechanics of Materials*, 31:131–139, 1999.

[49] M. Romano, M. Ryu, J. Morikawa, J.C. Batsale, and C. Pradere. Simultaneous microscopic measurements of thermal and spectroscopic fields of a phase change material. *Infrared Physics And Technology*, 76:65 – 71, 2016.

[50] T. Sakagami, T. Nishimura, T. Yamaguchi, and N. Kubo. A new full-field motion compensation technique for infrared stress measurement using digital image correlation. *Jounal of Strain Analysis*, 43:539–549, 2008.

[51] Thierry Sentenac and Remi Gilblas. Noise effect on interpolation equation for neai infrared thermography. *Metrologia*, mar 2013.

[52] J.C. Stinville, M.P. Echlin, D. Texier, F. Bridier, P. Bocher, and T.M. Pollock. Sub-grain scale digital image correlation by electron microscopy for polycrystalline materials during elastic and plastic deformation. *Experimental Mechanics*, 56(2):197 – 216, Feb 2016.

[53] S. Sun, M. Brandt, and M.S. Dargusch. Characteristics of cutting forces and chip formation in machining of titanium alloys. *International Journal of Machine Tools and Manufacture*, 49(7):561 – 568, 2009.

[54] G. Sutter, L. Faure, A. Molinari, N. Ranc, and V. Pina. An experimental technique for the measurement of temperature fields for the orthogonal cutting oin high-speed machining. *International Journal of Machine Tools and Manufacture*, 43(7):671–678, 2003.

[55] Z. Tang, J. Liang, Z. Xiao, and C. Guo. Large deformation measurement scheme for 3d digital image correlation method. *Optics and Lasers in Engineering*, 50(2):122–130, 2012.

[56] K. Triconnet, K. Derrien, F. Hild, and D. Baptiste. Parameter choice for optimized digital image correlation. *Optics and Lasers in Engineering*, 47:728–737, 2009.

[57] Asier Ugarte, Rachid M'Saoubi, Ainhara Garay, and P.J. Arrazola. Machining behaviour of ti-6al-4v and ti-5553 all0oys in interrupted cutting with pvd coated cemented carbide. *Procedia CIRP*, 1:202 – 207, 2012. Fifth CIRP Conference on High Performance Cutting 2012.

[58] P. Vacher, S. Dumoulin, F. Morestin, and S. Mguil-Touchal. Bidimensional strain measurement using digital images. *Proc. Inst. Mech. Eng.*, 213:811–817, 1999.

[59] F. Valiorgue, A. Brosse, P. Naisson, J. Rech, H. Hamdi, and J-M. Bergheau. Emissivity calibration for temperatures measurement using thermography in the context of machining. *Applied Thermal Engineering*, 58:321–326, 2013.

[60] Vincent Wagner, Arnaud Vissio, Emmanuel Duc, and Michele Pijolat. Relationship between cutting conditions and chips morphology during milling of aluminium al-2050. *The International Journal of Advanced Manufacturing Technology*, 82(9):1881–1897, Feb 2016.

[61] Qingqing Wang, Zhanqiang Liu, Bing Wang, Qinghua Song, and Yi Wan. Evolutions of grain size and microhardness during chip formation and machined surface generation for ti-6al-4v in high-speed machining. *The International Journal of Advanced Manufacturing Technology*, 82(9):1725–1736, Feb 2016.

[62] J. Weng, P. Cohen, and M. Herniou. Camera calibration with distortion model and accuracy evaluation. *IEEE Transactions on Pattern Analysis and Machine Intelligence*, 14(10):965–980, 1992.

[63] E.P. Whitenton. An introduction for machining researchers to measurement uncertainty sources in thermal images of metal cutting. *International Journal of Machining and Machinability of Materials*, 12(3):195 – 214, 2012.

[64] H. W. Yoon, D. W. Allen, and R. D. Saunders. Methods to reduce the size-of-source effect in radiometers. *Metrologia*, 42:89–96, April 2005.

[65] F. Zemzemi, J. Rech, W. Ben Salem, A. Dogui, and P. Kapsa. Identification of a friction model at tool/chip/workpiece interfaces in dry machining of aisi4142 treated steels. *Journal of Materials Processing Technology*, 209(8):3978 – 3990, 2009.

[66] D. Zhang, H. ZhaDing, and H. Ding. A study on the orthogonal cutting mechanism based on experimental determined displacement and temperature fields. *Procedia CIRP*, 46:35 – 38, 2016.

[67] X.P. Zhang, R. Shivpuri, and A.K. Srivastava. Role of phase transformation in chip segmentation during high speed machining of dual phase titanium alloys. *Journal of Materials Processing Technology*, 214(12):3048 – 3066, 2014.